

The Second Data Release of the INT Photometric H α Survey of the Northern Galactic Plane (IPHAS DR2)

Geert Barentsen^{1*}, H. J. Farnhill¹, J. E. Drew¹, E. A. González-Solares², R. Greimel³, M. J. Irwin², B. Miszalski⁴, C. Ruhland¹, P. Groot⁵, A. Mampaso^{6,7}, S. E. Sale⁸, A. A. Henden⁹, A. Aungwerojwit¹⁰, M. J. Barlow¹¹, P. J. Carter¹², R. L. M. Corradi^{6,7}, J. J. Drake¹³, J. Eisloffel¹⁴, J. Fabregat¹⁵, B. T. Gänsicke¹², N. P. Gentile Fusillo¹², S. Greiss¹², A. S. Hales¹⁶, S. Hodgkin², L. Huckvale¹⁷, J. Irwin¹³, R. King¹⁸, C. Knigge¹⁹, T. Kupfer⁵, E. Lagadec²⁰, D. J. Lennon²¹, J. R. Lewis², M. Mohr-Smith¹, R. A. H. Morris²², T. Naylor¹⁸, Q. A. Parker^{23,24,25}, S. Phillipps²¹, S. Pyrzas²⁶, R. Raddi¹², G. H. A. Roelofs¹³, P. Rodríguez-Gil^{6,7}, L. Sabin²⁷, S. Scaringi^{28,29}, D. Steeghs¹², J. Suso¹⁴, R. Tata^{6,7}, Y. C. Unruh³⁰, J. van Roestel⁵, K. Viironen³¹, J. S. Vink³², N. A. Walton², N. J. Wright¹, A. A. Zijlstra¹⁷.

¹School of Physics, Astronomy & Mathematics, University of Hertfordshire, College Lane, Hatfield, Hertfordshire, AL10 9AB, U.K.

²Institute of Astronomy, University of Cambridge, Madingley Road, Cambridge, CB3 OHA, U.K.

³IGAM, Institute of Physics, University of Graz, Universitätsplatz 5, 8010 Graz, Austria.

⁴South African Astronomical Observatory & SALT Foundation, P.O. Box 9, Observatory, 7935 Cape Town, South Africa.

⁵Afdeling Sterrenkunde, Radboud Universiteit Nijmegen, Faculteit NWI, Postbus 9010, 6500 GL Nijmegen, The Netherlands.

⁶Instituto de Astrofísica de Canarias, Vía Láctea, s/n, La Laguna, E-38205, Santa Cruz de Tenerife, Spain.

⁷Departamento de Astrofísica, Universidad de La Laguna, La Laguna, E-38204, Santa Cruz de Tenerife, Spain.

⁸Rudolf Peierls Centre for Theoretical Physics, Keble Road, Oxford, OX1 3NP, U.K.

⁹AAVSO, 49 Bay State Road, Cambridge, MA 02138, USA.

¹⁰Department of Physics, Faculty of Science, Naresuan University, Phitsanulok 65000, Thailand.

¹¹University College London, Department of Physics & Astronomy, Gower Street, London WC1E 6BT, U.K.

¹²Department of Physics, University of Warwick, Gibbet Hill Road, Coventry, CV4 7AL, U.K.

¹³Harvard-Smithsonian Center for Astrophysics, 60 Garden Street, Cambridge, MA 02138, U.S.A.

^{14–32} (affiliations 14 through 32 are given in the source file)

Current draft typeset 31 July 2014

ABSTRACT

The INT/WFC Photometric H α Survey of the Northern Galactic Plane (IPHAS) is a 1800 deg² imaging survey covering Galactic latitudes $|b| < 5^\circ$ and longitudes $\ell = 30^\circ$ to 215° in the r , i and H α filters using the Wide Field Camera (WFC) on the 2.5-metre Isaac Newton Telescope (INT) in La Palma. We present the first quality-controlled and globally-calibrated source catalogue derived from the survey, providing single-epoch photometry for 219 million unique sources across 92 per cent of the footprint. The observations were carried out between 2003 and 2012 at a median seeing of 1.1 arcsec (sampled at 0.33 arcsec/pixel) and to a mean 5σ -depth of 21.2 (r), 20.0 (i) and 20.3 (H α) in the Vega magnitude system. We explain the data reduction and quality control procedures, describe and test the global re-calibration, and detail the construction of the new catalogue. We show that the new calibration is accurate to 0.03 mag (rms) and recommend a series of quality criteria to select accurate data from the catalogue. Finally, we demonstrate the ability of the catalogue’s unique ($r - \text{H}\alpha$, $r - i$) diagram to (i) characterise stellar populations and extinction regimes towards different Galactic sightlines and (ii) select and quantify H α emission-line objects. IPHAS is the first survey to offer comprehensive CCD photometry of point sources across the Galactic Plane at visible wavelengths, providing the much-needed counterpart to recent infrared surveys.

Key words: catalogues, surveys, stars: emission line, Be, Galaxy: stellar content

1 INTRODUCTION

The INT/WFC Photometric H α Survey of the Northern Galactic Plane (IPHAS; Drew et al. 2005) is providing new insights into the contents and structure of the disk of the Milky Way. This large-scale programme of observation – spanning a decade so far and using more than 300 nights in competitive open time at the Isaac Newton Telescope (INT) in La Palma – aims to provide the digital update to the photographic northern H α surveys of the mid-20th century (see Kohoutek & Wehmeyer 1999). By increasing the sensitivity with respect to these preceding surveys by a factor ~ 1000 (7 magnitudes), IPHAS can expand the limited bright samples of Galactic emission line objects previously available into larger, deeper, and more statistically-robust samples that will better inform our understanding of the early and late stages of stellar evolution. Since the publication of the Initial Data Release (IDR; González-Solares et al. 2008), these aims have begun to be realised through a range of published studies including: a preliminary catalogue of candidate emission-line objects (Witham et al. 2008); discoveries of new symbiotic stars (Corradi et al. 2008, 2010; Corradi et al. 2011; Rodríguez-Flores et al. 2014); new cataclysmic variables (Witham et al. 2007; Wesson et al. 2008; Aungwejwit et al. 2012); new groups of young stellar objects (Vink et al. 2008; Barentsen et al. 2011; Wright et al. 2012); new classical Be stars (Raddi et al. 2013); along with discoveries of new supernova remnants (Sabin et al. 2013) and new and remarkable planetary nebulae (Mampaso et al. 2006; Viironen et al. 2009a,b; Sabin et al. 2010; Corradi et al. 2011; Viironen et al. 2011; Sabin et al. 2014).

Over the years it has become apparent that the legacy of IPHAS will reach beyond these traditional H α applications of identifying emission-line stars and nebulae. Through the provision of r and i broadband photometry alongside narrowband H α data, IPHAS has created the opportunity to study Galactic Plane populations in a new way. For example, the survey's unique ($r - \text{H}\alpha$, $r - i$) colour-colour diagram has been shown to provide simultaneous constraints on intrinsic stellar colour and interstellar extinction (Drew et al. 2008). This has opened the door to a wide range of Galactic science applications, including the mapping of extinction across the Plane in three dimensions and the probabilistic inference of stellar properties (Sale et al. 2009, 2010; Giannanco et al. 2011; Sale 2012; Barentsen et al. 2013; Sale et al. 2014). In effect, the availability of narrowband H α alongside r and i magnitudes provides coarse spectral information for huge samples of stars which are otherwise too faint or numerous to be targeted by spectroscopic surveys (cf. the use of Stromgren $uvbyH\beta$ photometry at blue wavelengths). For such science applications to succeed, however, it is vital that the imaging data are transformed into a homogeneously-calibrated photometric catalogue, in which quality problems and duplicate detections are flagged.

When the previous release – the IDR – was created in late 2007, just over half of the survey footprint was covered and the data were insufficiently complete to support a homogeneously calibrated source catalogue. The goal of this paper is to present the next release, which supersedes the IDR by including a global re-calibration and by taking the coverage up to 92 per cent of the survey area. In

Table 1. Key properties of IPHAS DR2.

| Property | Value |
|-------------------------------------|---|
| Telescope | 2.5m Isaac Newton Telescope |
| Instrument | Wide Field Camera (WFC) |
| Detectors | Four 2048 \times 4100 pixel CCD's |
| Pixel scale | 0.33 arcsec/pixel |
| Filters | r , i , H α |
| Filter properties | See Table 2 |
| Magnitude system | Vega |
| Exposure times | 30 s (r), 10 s (i), 120 s (H α) |
| Saturation limit | 13 (r), 12 (i), 12.5 (H α) |
| Detection limit (5 σ , mean) | 21.2 (r), 20.0 (i), 20.3 (H α) |
| PSF FWHM (median) | 1.1'' (r), 1.0'' (i), 1.1'' (H α) |
| Survey area | $\sim 1860 \text{ deg}^2$ |
| Footprint boundaries | $-5^\circ < b < +5^\circ$, $29^\circ < \ell < 215^\circ$ |
| Observing period | August 2003 - November 2012 |
| Website | www.iphas.org |

this work we (i) explain the data reduction and quality control procedures that were applied, (ii) describe and test the new photometric calibration, and (iii) detail the construction of the source catalogue and demonstrate its use.

In §2 we start by recapitulating the key points of the survey observing strategy. In §3 we describe the data reduction and quality control procedures. In §4 we explain the global re-calibration, in which we draw upon the AAVSO Photometric All-Sky Survey (APASS) and test our results against the Sloan Digital Sky Survey (SDSS). In §5 we explain how the source catalogue was compiled. In §6 we discuss the properties of the catalogue and in §7 we demonstrate the scientific exploitation of the colour/magnitude diagrams. Finally, in §8 we discuss access to the catalogue and an online library of reduced images. The paper ends with conclusions in §9 where we also outline our future ambitions.

2 OBSERVATIONS

The detailed properties of the IPHAS observing programme have been presented before by Drew et al. (2005) and González-Solares et al. (2008). To set the stage for this release, we recap some key points in this section (see Table 1 for a summary). IPHAS is an imaging survey of the Galactic Plane north of the celestial equator, from which photometry in Sloan r and i is extracted along with narrowband H α . It is carried out using the Wide Field Camera (WFC) on the 2.5-metre INT in La Palma. It is the first digital survey to offer comprehensive optical CCD photometry of point sources in the Galactic Plane; the footprint spans a box of roughly 180 by 10 degrees, covering Galactic latitudes $-5^\circ < b < +5^\circ$ and longitudes $30^\circ < \ell < 215^\circ$.

The WFC is a mosaic of 4 CCDs that captures a sky area of close to 0.29 deg^2 at a pixel scale of 0.33 arcsec/pixel. To cover the Northern Plane with some overlap, the survey area was divided into 7,635 telescope pointings. Each of these pointings is accompanied by an offset position displaced by +5 arcmin in Dec and +5 arcmin in RA, to deal with inter-CCD gaps, detector imperfections, and to enable quality checks. An example footprint of a pointing

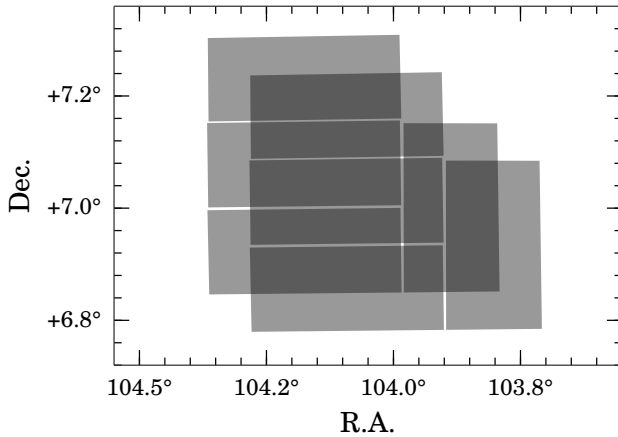


Figure 1. Example footprint of a pointing and its offset position. Each field in the survey is accompanied by an offset field at 5' West and South to deal with gaps between the CCDs. This unit of observation is called a *field pair*, which is observed in all three filters within a span of 10 minutes. The WFC is a mosaic of four CCDs, and hence a field pair is composed of eight CCD frames. In this example, each CCD is plotted as a semi-transparent grey rectangle to highlight the overlap regions. Note that the L-shaped arrangement of the CCD mosaic allows nearly the entire field to be captured using just two pointings, apart from two $\sim 10''$ -wide squares which are located where inter-CCD gaps overlap.

and its offset position is shown in Fig. 1. Hence, the basic unit of observation amounts to 2×3 exposures, in which each of the 3 survey filters is exposed at 2 offset sky positions within, typically, an elapsed time of 10 minutes. We shall refer to the unit of 3 exposures at the same position as a *field*, and the combination of two fields at a small offset as a *field pair*. Altogether, the survey contains 15,270 fields grouped into 7,635 field pairs. To achieve the desired survey depth of 20th magnitude or fainter in each filter, the exposure times were set at 120 s ($H\alpha$), 30 s (r) and 10 s (i) in the vast majority of the survey observations.¹

Data-taking began in the second half of 2003, and every field had been observed at least once by the end of 2008. At that time only 76 per cent of the field pairs satisfied our minimum quality criteria, however. The problems affecting the 24 per cent falling below survey standard were, most commonly: variable cloud cover; poor seeing; technical faults (the quality criteria will be detailed in the next section). Since then, a programme of repeat observations has been in place to improve data quality. As a result, 92 per cent of the survey footprint now benefits from quality-approved data. The most recent observations included in this release were obtained in November 2012.

Fig. 2 shows the footprint of the quality-approved observations included in this work. The fields which remain missing – covering 8 per cent of the survey area – are predominantly located towards the Galactic anti-centre at $\ell > 120^\circ$. Fields at these longitudes are mainly accessed from

¹ The r -band exposure time was 10s instead of 30s in the first months of data taking. Since October 2010, the i -band exposure time has been increased from 10s to 20s to bypass a sporadic exposure timing bug that affects the WFC.

La Palma in the months of November–December, which is when the La Palma weather and seeing conditions are often poor, forcing many (unsuccessful) repeat observations. To enable the survey to be brought to completion, a decision was made recently to limit repeats in this area to individual fields requiring replacement, i.e. fresh observations in all 3 filters may only be obtained at one of the two offset positions. The catalogue is structured such that it is clear where contemporaneous observations of both halves of a field pair are available.

3 DATA REDUCTION AND QUALITY CONTROL

3.1 Initial pipeline processing

All raw IPHAS data were transferred to the Cambridge Astronomical Survey Unit (CASU) for initial processing and archiving. The procedures used by CASU were originally devised for the INT Wide Field imaging Survey (WFS; McMahon et al. 2001; Irwin et al. 2005), which was a 200 deg² **extragalactic** survey programme carried out between 1998 and 2003. Because IPHAS uses the same telescope and camera combination, we have been able to benefit from the existing WFS pipeline. A description of the processing steps is found in Irwin & Lewis (2001). Its application to IPHAS has previously been described by Drew et al. (2005) and González-Solares et al. (2008), and the source code is available on-line². In brief, the pipeline takes care of bias subtraction, linearity correction, flat-fielding, gain correction and de-fringing.

Object detection and parametrisation is then carried out using the standard methods in use by CASU, which can be summarised in four steps (a discussion on each of these steps and related points can be found in Irwin 1985, 1997):

(i) The local sky background is estimated by computing the sigma-clipped median intensity in a grid of 64×64 pixel bins across the image, which is robust against contaminating sources. Bilinear interpolation is then used to obtain an estimate of the background level at each pixel.

(ii) Objects, or blends of objects, are detected by identifying groups of 4 or more neighbouring pixels in which the intensity exceeds the background level by at least 1.25σ .

(iii) The object are parametrised: positions are obtained by computing the intensity-weighted isophotal centre-of-gravity of each object, and photometry is obtained by measuring the intensity in a series of soft-edged circular apertures of increasing diameter ($1''.2$, $2''.3$, $3''.3$, $4''.6$ and $6''.6$). Objects are also classified morphologically – stellar, extended or noise – based on their intensity as a function of aperture size.

(iv) The parametrisation of overlapping objects is refined by simultaneous fitting of soft-edged apertures to each blend, effectively carrying out pro-

² <http://casu.ast.cam.ac.uk/surveys-projects/software-release>

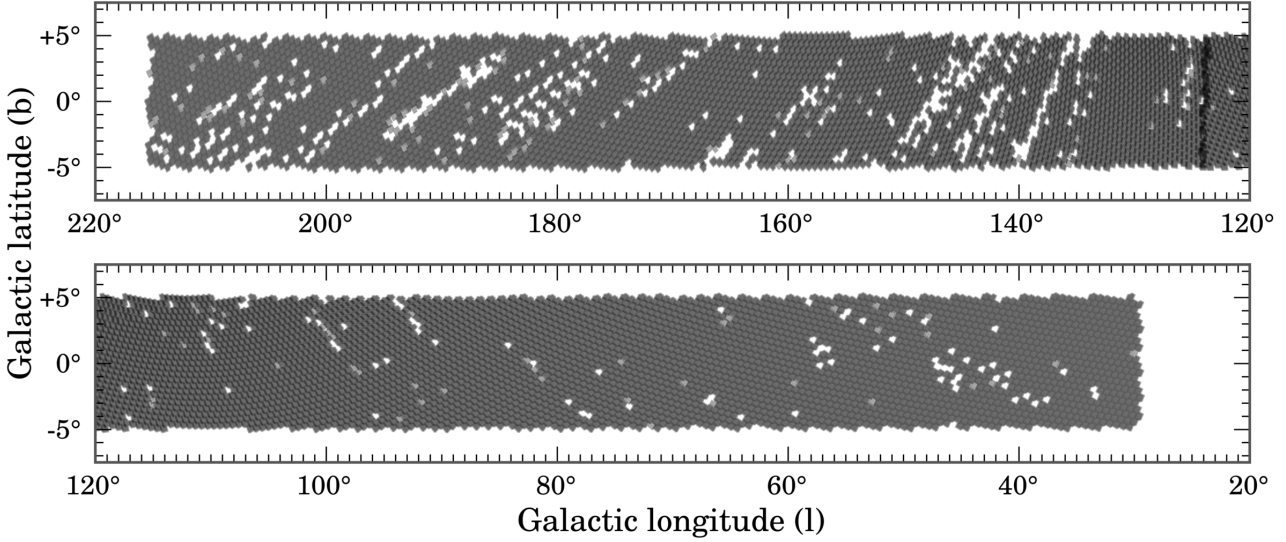


Figure 2. Survey area showing the footprints of all the quality-approved IPHAS fields which have been included in this data release. The area covered by each field has been coloured black with a semi-transparent opacity of 20 per cent, such that regions where fields overlap are darker. The IPHAS strategy is to observe each field twice with a small offset, and hence the vast majority of the area is covered twice (dominant grey colour). There are small overlaps between all the neighbouring fields which can be seen as a honeycomb pattern of dark grey lines across the survey area. Regions with incomplete data are apparent as white gaps (no data) or in light grey (indicating that one offset is missing). The dark vertical strip near $\ell \approx 125^\circ$ is an arbitrary consequence of the tiling pattern, which was populated starting from 0h in Right Ascension.

file fitting where it is necessary. We note that the parametrisation of these blended objects is naturally less reliable than that of single, unconfused sources, which is why they are flagged in the catalogue (to be explained in §5).

Having carried out object detection, the astrometric calibration is then determined. The solution starts with a rough World Coordinate System (WCS) based on the known telescope and camera geometry, using a Zenithal Polynomial projection (ZPN; Calabretta & Greisen 2002) to model the field distortion of the camera. The parameters of this solution are then progressively refined by fitting against the Two-Micron All Sky Survey (2MASS; Skrutskie et al. 2006). We did not include proper motion information during this step, because each CCD typically contains hundreds of 2MASS reference stars. The resulting fit has previously been shown to deliver results which are internally consistent to better than $0.^{\prime\prime}1$ across the detector (González-Solares et al. 2008).

An external validation of the astrometry has been carried out by comparing our positions against the United States Naval Observatory CCD Astrograph Catalog (UCAC4; Zacharias et al. 2013). Fig. 3 shows the distribution of the position offsets against UCAC4 computed for 1.3 million stars in the magnitude range $13 < r < 15$, which is the range where both surveys overlap and where the formal mean error of UCAC4 is better than 50 mas (Zacharias et al. 2010). We find the mean position offset to be $0.^{\prime\prime}09 \pm 0.^{\prime\prime}07$, which is satisfactory for our purposes. We note that both UCAC4 and 2MASS –

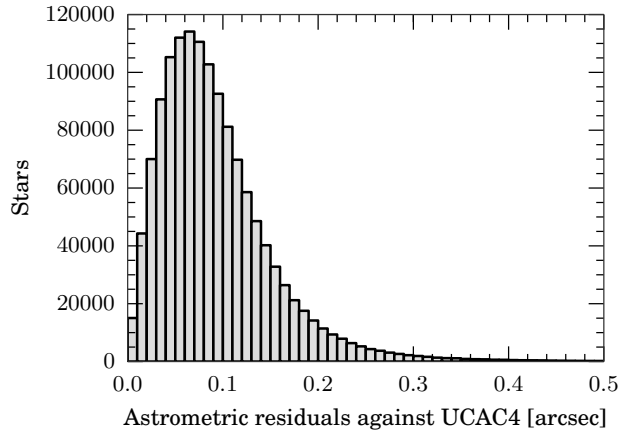


Figure 3. Distribution of the position offsets of stars which appear both in IPHAS DR2 and UCAC4 within a cross-matching distance of $1''$. The residuals were computed for the 1.3 million stars in the IPHAS catalogue which are not blended, not saturated, and fall in the magnitude range $13 < r < 15$. The mean and standard deviation of this distribution equals $0.^{\prime\prime}09 \pm 0.^{\prime\prime}07$.

and hence also IPHAS – are calibrated in the International Celestial Reference System (ICRS).

At the time of preparing DR2, the pipeline had processed 74,195 single-band IPHAS exposures in which a total of 1.9 billion *candidate* detections were made. This total inevitably includes spurious objects, artefacts and duplicate detections; in §5 we will explain how these have been removed or flagged in the final catalogue.

The entire data set – comprising 2.5 terabyte of FITS files – was then transferred to the University of Hertfordshire for the purpose of transforming the raw detection tables into a proper source catalogue which (i) is quality-controlled, (ii) is homogeneously calibrated, and (iii) contains user-friendly columns and warning flags. It is these post-processing steps which distinguish this release from the IDR, which (i) enforced less stringent quality limits, (ii) did not offer a global calibration, and (iii) provided a catalogue in which duplicate detections of unique sources were not flagged. These improvements are explained next.

3.2 Quality control

Observing time for IPHAS is obtained on a semester-by-semester basis through the open time allocation committees of the Isaac Newton Group of telescopes. The survey is allocated specific observing dates rather than particular observing conditions. In consequence, data were acquired under a large range of atmospheric conditions. Data taken under unsuitable conditions have been rejected using seven quality criteria, which ensure a good and homogeneous level of quality across the data release:

(1) *Depth*. We discarded any exposures for which the 5σ limiting magnitude³ was brighter than 20th magnitude in the r -band or brighter than 19th in i or $\text{H}\alpha$. Such data were typically obtained during poor weather or full moon. Most observations were significantly better than these limits. Fig. 4 presents the distribution of limiting magnitudes for all quality-approved fields; the mean depths and standard deviations are 21.2 ± 0.5 (r), 20.0 ± 0.3 (i) and 20.3 ± 0.3 ($\text{H}\alpha$). The depth achieved depended most strongly on the presence of the moon, which was above the horizon during 62 per cent of the observations. The great range in sky brightness this produced is behind the wide and bi-modal shape of the r -band limiting magnitude distribution (top panel in Fig. 4). In contrast, the depths attained in i and $\text{H}\alpha$ are less sensitive to moonlight, leading to narrower magnitude limit distributions (middle and bottom panels in Fig. 4). To a lesser extent, the wide spread in the r -band depth is also explained by the shorter exposure time that was used for this band during the first months of data-taking.

(2) *Ellipticity*. The ellipticity of a point source, defined as $e = 1 - b/a$ with b the semi-minor and a the semi-major axis, is a morphological measure of the elongation of the Point Spread Function (PSF). It is expected to be zero (circular) in a perfect imaging system, but it is slightly non-zero in any real telescope data due to optical distortions and tracking errors. Indeed, it is worth noting that IPHAS data have been collected from unguided exposures that rely entirely on the INT’s tracking capability. The mean ellipticity

³ We defined the 5σ limiting magnitude as the magnitude which an imaginary point source would have if its flux equalled five times the level of the noise in the sky background. The sky noise was estimated using a robust MAD estimator for noise scaled to equivalent Gaussian standard deviation, ie. = $\text{MAD} \times 1.48$, after removing large scale sky background variations. (MAD = Median of the Absolute Deviations about the median.)

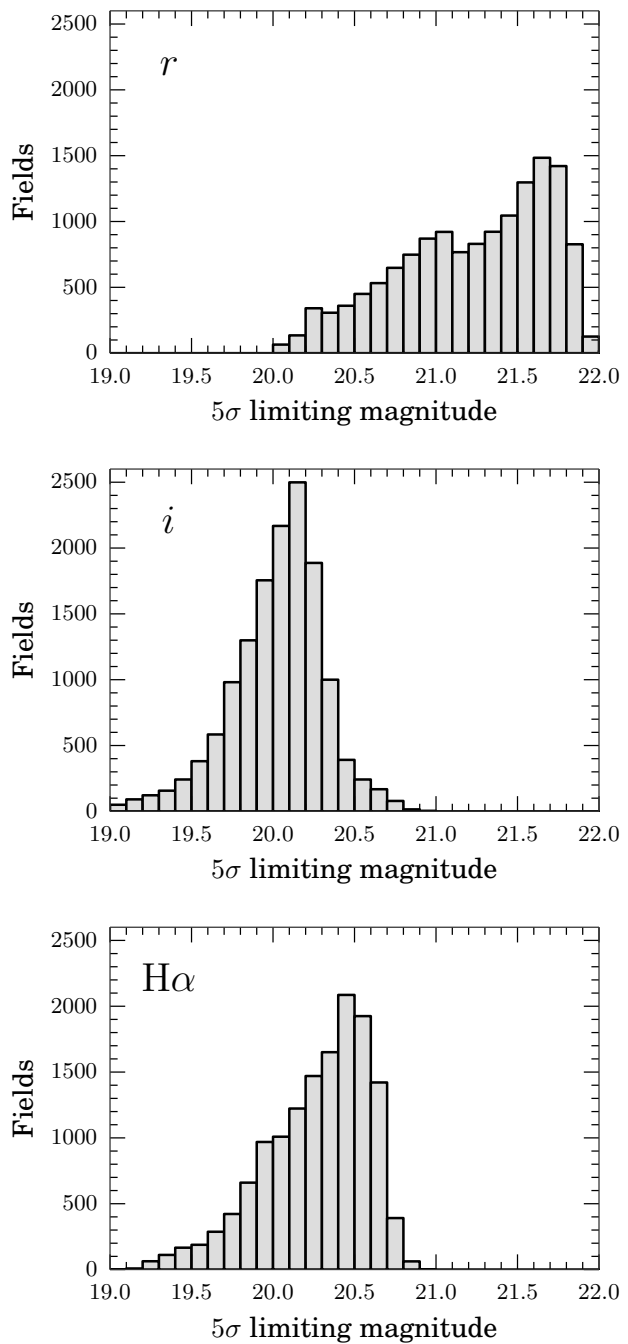


Figure 4. Distribution of the 5σ limiting magnitude across all quality-approved survey fields for r (top), i (middle) and $\text{H}\alpha$ (bottom). Fields with a limiting magnitude brighter than 20th (r) or 19th ($\text{H}\alpha$, i) were rejected from the data release. The r -band depth is most sensitive to the presence of the moon above the horizon: this is the main reason for the wide, bi-modal character of its distribution.

measured in the data is 0.09 ± 0.04 . There have been sporadic episodes with higher ellipticities due to mechanical glitches in the telescope tracking system. As a result, 3 per cent of our images show an average ellipticity across the detectors which is worse than $e > 0.2$. The inspection of these examples revealed no evidence for degraded

photometry up to ellipticities less than 0.3. In fact high ellipticities are naturally correlated with superior seeing. We did however exclude a small number of exposures which exceeded $e > 0.3$.

(3) *Seeing.* The original survey goal was to obtain data at a resolution better than 1.7 arcsec, as evaluated by measuring the average PSF Full Width at Half Maximum (FWHM) across the detectors. This target is currently attained across 86 per cent of the footprint. To increase the sky area offered by the data release slightly, we have decided to accept data obtained with FWHM up to 2.5 arcsec. Fig. 5 presents the distribution of the PSF FWHM for the approved fields. In the r -band, 90 per cent is better than 1.5 arcsec, 50 per cent is better than 1.1 arcsec, and 10 per cent is better than 0.8 arcsec. In §5 we will explain that the photometry compiled in the source catalogue is normally derived from the field with the best-available seeing for a given object, and that the FWHM measurement is available as a column in the catalogue.

(4) *Photometric repeatability.* The IPHAS field-pair observing strategy normally ensures that every pointing is immediately followed by an offset pointing at a displacement of +5 arcmin in Dec and +5 arcmin in RA. This allows pairs of images to be checked for the presence of clouds or electronic noise. To exploit this information, the overlap regions of all field pairs were systematically cross-matched to verify the consistency of the photometry for stars observed in both pointings. We automatically rejected field pairs in which more than 2 per cent of the stars showed an inconsistent measurement at the level of 0.2 mag, or more than 25 per cent were inconsistent at the level of 0.1 mag. These limits were set empirically after inspecting the images and photometry by eye.

(5) *Visual examination.* Images, colour mosaics, and the associated photometric colour/magnitude diagrams were inspected by a team of 20 survey members, such that each image in the data release was looked at by at least three different pairs of eyes. Images affected by clouds or extreme levels of scattered moonlight were flagged, investigated, and excluded from the release if deemed necessary.

(6) *Source density mapping.* Spatial maps showing the number density of the detected sources down to 20th magnitude were created to verify the health of the data and to check for unexpected artefacts. In particular, we created density maps which showed the number of *unique* sources obtained by cross-matching the detection tables of all three bands with a maximum matching distance of 1 arcsec. This was effective for revealing fields with an inaccurate astrometric solution in one of the bands, which were subsequently corrected.

(7) *Contemporaneous field data.* Finally, only exposures which are part of a sequence of three consecutive images of the same field ($\text{H}\alpha$, r , i) were considered for inclusion in the release. This ensures that the three bands for a given field are observed contemporaneously – nearly always within 5 minutes of each other. We note that the source catalogue details the exact epoch at the start of each exposure (columns $r\text{MJD}$, $i\text{MJD}$, $h\text{aMJD}$).

The above criteria were satisfied by at least one observing attempt for 14,115 out of the 15,270 planned fields (92 per cent). In some cases more than one successful attempt to observe a field was available due to stricter quality criteria

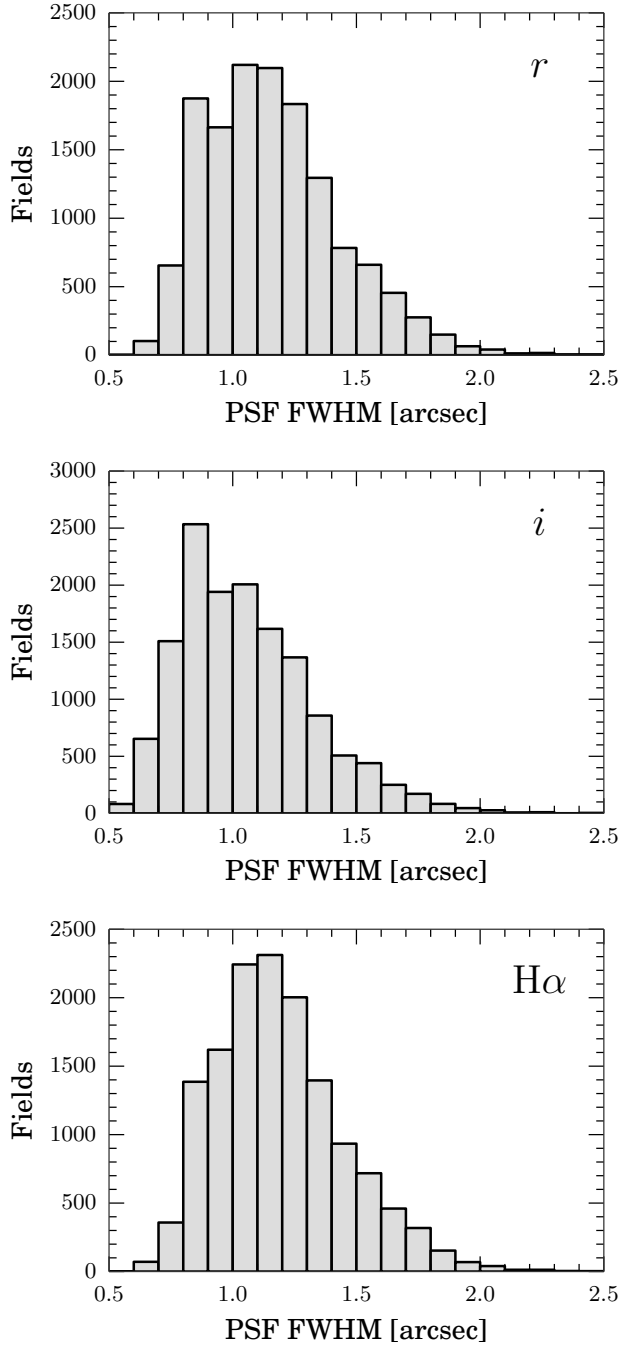


Figure 5. Distribution of the PSF FWHM for all the quality-approved fields included in the release, measured in r (top), i (middle) and $\text{H}\alpha$ (bottom). The PSF FWHM measures the effective image resolution that arises from the combination of atmospheric and dome seeing.

being applied in the initial years of the survey. In such cases, only the attempt with the best seeing and depth has been selected for inclusion in the catalogue, in order to deliver the most accurate measurement at a single epoch.

We note that some of the excluded data may nevertheless be useful for e.g. time-domain studies of bright stars. The discarded data is available through our website, but will be ignored in the remainder of this work.

4 PHOTOMETRIC CALIBRATION

Having obtained a quality-approved set of observations, we now turn to the challenge of placing the data onto a uniform photometric scale.

4.1 Provisional nightly calibration

For the purpose of providing an initial calibration of the r and i broadband fluxes, photometric standard fields were observed every night. The standards were chosen from a list based on the Landolt (1992) and Stetson (<http://cadcwww.dao.nrc.ca/standards>) objects. Two or three standard fields were observed during the evening and morning twilight, and at intervals of 2–3 hours throughout the night. The CASU pipeline automatically identified the observed standards and used them to determine a sigma-clipped average zeropoint MAGZPT for each night and filter, such that the number counts DN in the pipeline-corrected CCD frames relate to a magnitude m as:

$$m = \text{MAGZPT} - 2.5 \log_{10}(DN/\text{EXPTIME}) - \text{EXTINCT} \cdot (\text{AIRMASS} - 1) - \text{APCOR} - \text{PERCORR}, \quad (1)$$

where EXPTIME is the exposure time in seconds, EXTINCT is the atmospheric extinction coefficient (set in the pipeline at 0.09 for r and 0.05 for i as representative averages for the telescope site), AIRMASS is the normalised optical path length through the atmosphere and APCOR is a correction for the flux lost outside of the aperture used (we adopt a 2''.3-diameter circular aperture by default). Finally, percorr is a term used to correct for the small difference in internal gain computed using the twilight flats compared to the much redder typical astronomical objects. It is estimated by making a robust average of the dark sky levels measured on each detector during an observing run (the correction is 0.01 ± 0.01 on average in i and 0.00 ± 0.00 in r and $\text{H}\alpha$). All these quantities correspond to header keywords in the FITS files produced by the CASU pipeline.

The broadband zeropoints were determined such that the resulting magnitude system refers to the spectral energy distribution (SED) of Vega as the zero colour object. Colour equations were used to transform between the IPHAS passbands and the Johnson-Cousins system of the published standard star photometry. The entire procedure has been found to deliver zeropoints which are accurate at the level of 1–2 per cent in stable photometric conditions (González-Solares et al. 2011).

Unlike the broadbands, standard-star photometry is not available in the literature for the $\text{H}\alpha$ passband and hence there is no formally recognised flux scale for it. We can specify here, however, that the detected flux for Vega in the IPHAS $\text{H}\alpha$ filter is 3.14 magnitudes less than the flux captured by the much broader r band (González-Solares et al. 2008). Hence to assure that $(r - \text{H}\alpha) = 0$ for Vega, we set the zeropoint for the narrowband to be:

$$\text{MAGZPT}_{\text{H}\alpha} = \text{MAGZPT}_r - 3.14. \quad (2)$$

For reference, Table 2 details the flux of Vega in the IPHAS

Table 2. Mean monochromatic flux of Vega in the IPHAS filter system, defined as $\langle f_\lambda \rangle = \int f_\lambda(\lambda)S(\lambda)\lambda d\lambda / \int S(\lambda)\lambda d\lambda$, where $S(\lambda)$ is the photon response function (which includes atmospheric transmission, filter transmission and CCD response) and $f_\lambda(\lambda)$ is the CALSPEC SED for Vega (Bohlin 2014). For reference, we also provide the filter equivalent width $\text{EW} = \int S(\lambda)d\lambda$, the mean photon wavelength $\lambda_0 = \int S(\lambda)\lambda d\lambda / \int S(\lambda)d\lambda$, and the pivot wavelength $\lambda_p = \sqrt{\int S(\lambda)\lambda d\lambda / \int \frac{S(\lambda)}{\lambda} d\lambda}$. These notations follow the definitions by Bessell & Murphy (2012). After multiplying $\langle f_\lambda \rangle$ by the EW, we find that the detected flux for Vega in $\text{H}\alpha$ is 3.14 magnitudes less than that received in r .

| Filter | $\langle f_\lambda \rangle$ [erg cm $^{-2}$ s $^{-1}$ Å $^{-1}$] | EW [Å] | λ_0 [Å] | λ_p [Å] |
|------------------|--|-----------|--------------------|--------------------|
| r | 2.47×10^{-9} | 785.6 | 6223 | 6211 |
| $\text{H}\alpha$ | 1.81×10^{-9} | 59.6 | 6568 | 6568 |
| i | 1.30×10^{-9} | 759.9 | 7674 | 7661 |

filter system. Data on the throughput curves of the bands can be obtained from the Isaac Newton Group website⁴.

4.2 Global re-calibration

Despite the best efforts made to obtain a nightly calibration, large surveys naturally possess field-to-field variations due to atmospheric changes during the night and imperfections in the pipeline or the instrument (e.g. the WFC is known to suffer from sporadic errors in the timing of exposures). This is demonstrated in Fig. 6a, where we show the combined colour-colour diagram for nearly 3,000 fields across an area of 400 deg 2 . The main locus of stars is poorly defined in the diagram due to the presence of incorrectly calibrated fields, which need to be corrected during a global re-calibration step. The application of such a procedure, to be explained below, has revealed that the error in our initial nightly calibration exceeded 0.1 mag in 12 per cent of the fields, and even exceeded 0.5 mag in 0.7 per cent. For comparison, Fig. 6b demonstrates the improvement in the colour-colour diagram after re-calibrating.

Notable past examples of surveys which required global re-calibration include 2MASS (Nikolaev et al. 2000), SDSS (Padmanabhan et al. 2008) and the Panoramic Survey Telescope And Rapid Response System survey (Pan-STARRS; Schlafly et al. 2012), which all achieved photometry that is globally consistent to within 0.01–0.02 mag after re-calibration.

Surveys which observe identical stars at different epochs can use the repeat measurements to ensure a homogeneous calibration. For example, 2MASS attained its global calibration by observing two standard fields each hour, allowing zeropoint variations to be tracked over short timescales (Nikolaev et al. 2000). Alternatively, the SDSS and PanSTARRS surveys could benefit from revisiting regions in their footprint to carry out a so-called *ubercalibration*.

⁴ <http://catserver.ing.iac.es/filter/list.php?instrument=WFC> where the filters are named WFCH6568, WFCsloanR and WFCsloanI

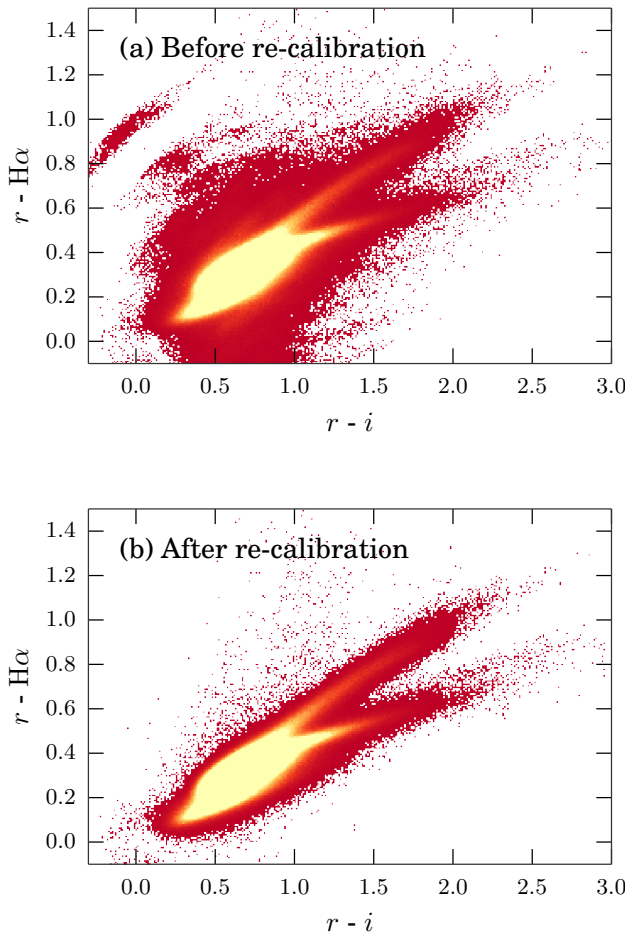


Figure 6. IPHAS ($r - H\alpha$, $r - i$) colour-colour diagram covering an area of 400 deg^2 , shown before (panel a) and after (panel b) re-calibration. Both figures were created by combining the stars detected across all 2,801 quality-approved fields which are located towards the Galactic anti-centre ($160^\circ < \ell < 200^\circ$). The diagrams are plotted as 2D-histograms which show the density of sources in bins of 0.01-by-0.01 mag; bins containing 1 to 200 sources are coloured red, while bins containing more than 400 sources are bright yellow. The diagrams include all stars brighter than $r < 18$ which were classified by the pipeline as ‘a10point’ (indicating a high-significance point source detection with accurate photometry in all bands, to be explained in §6.2). The objects which are seen to fall above the locus of stars *after* re-calibration are likely to be genuine $H\alpha$ emission-line objects.

tion⁵ procedure, in which repeat measurements of stars in different nights are used to fit the calibration parameters (Ivezić et al. 2007; Padmanabhan et al. 2008; Schlafly et al. 2012).

Unfortunately these schemes cannot be applied directly to IPHAS for two reasons. First, the survey was carried

⁵ ‘ubercalibration’ refers to the name of the code used to re-calibrate SDSS photometry. It is an anglicised version of the German word ‘überkalibration’, which was reportedly chosen because the initial authors, Schlegel and Finkbeiner, both have German-sounding names (Finkbeiner 2010).

out in competitively-allocated observing time on a common-user telescope, rendering the 2MASS approach of observing standards at a high frequency prohibitively expensive (it does not help that standard fields are very scarce within the Galactic Plane). Second, IPHAS is not specified as a variability survey, with the result that stars are not normally observed at more than one epoch, unless they happen to fall within a narrow overlap region between two neighbouring field pairs.

We have found the information contained in our narrow overlap regions to be insufficient to constrain the calibration parameters. This is because photometry at the extreme edges of the WFC – where neighbouring fields overlap – is prone to systematics at the level of 1–2 per cent. The cause of these errors is thought to include the use of twilight sky flats in the pipeline, which are known to be imperfect for calibrating stellar photometry due to stray light and vignetting (e.g. Manfroid 1995). Moreover, the illumination correction in the overlap regions is more affected by a radial geometric distortion in the WFC, which causes the pixel scale to increase as the edges are approached (González-Solares et al. 2011). Although these systematics are reasonably small within a single field, they can accumulate during a re-calibration process, causing artificial zeropoint gradients across the survey unless controlled by other external constraints.

For these reasons, we have not depended on an ubercalibration-type scheme alone, but have opted to involve an external reference survey – where available – to bring the majority of our data onto a homogeneous calibration.

4.2.1 Correcting zeropoints using APASS

We have been able to benefit from APASS (<http://www.aavso.org/apass>) to bring most of the survey onto a uniform scale. Since 2009, APASS has been using two 20 cm-astrographs to survey the entire sky down to ~ 17 th magnitude in five filters which include Sloan r and i (Henden et al. 2012). The most recent catalogue available at the time of preparing this work was APASS DR7, which provides a good coverage across \sim half of the IPHAS footprint. The overlap regions are shown in Fig. 7. The photometric accuracy of APASS is currently estimated to be at the level of 3 per cent, which is significantly better than the original nightly calibrations of IPHAS which are only accurate to ~ 10 per cent when compared to APASS (Table 3). APASS achieves its uniform accuracy by measuring each star at least two times in photometric conditions, along with ample standard fields, benefiting from the large 3-by-3 degrees field of view of its detectors.

With the aim of bringing IPHAS to a similar accuracy of 3 per cent, we used the APASS catalogue to identify and adjust the calibration of all IPHAS fields which showed a magnitude offset larger than 0.03 mag against APASS. Experience of re-running the calibration and testing the results showed us that it was inadvisable to tune more finely the match for IPHAS data obtained in what were generally the most photometric nights. To this end, the r - and i -band detection tables of each IPHAS field were cross-matched against the APASS DR7 catalogue using a maximum matching distance of 1 arcsec. The magnitude range was limited to $13 < r_{\text{APASS}} < 16.5$ and $12.5 < i_{\text{APASS}} < 16.0$ in order to avoid sources brighter than the IPHAS saturation limit

Table 3. Magnitude offsets for objects cross-matched between IPHAS and APASS/SDSS *before* the global re-calibration was carried out. We characterise the distribution of the offsets, which is approximately Gaussian in each case, by listing the mean and the standard deviation values. We remind the reader that transformations were applied to the APASS and SDSS magnitudes to bring them into the Vega-based IPHAS system prior to computing the offsets.

| Before re-calibration | Mean | σ |
|-----------------------|--------|----------|
| r (IPHAS - APASS) | +0.014 | 0.104 |
| i (IPHAS - APASS) | +0.007 | 0.108 |
| r (IPHAS - SDSS) | +0.016 | 0.088 |
| i (IPHAS - SDSS) | +0.010 | 0.089 |

Table 4. Same as Table 3, but computed *after* the global re-calibration was carried out. The mean and standard deviation values of the offsets have improved significantly.

| After re-calibration | Mean | σ |
|----------------------|--------|----------|
| r (IPHAS - APASS) | +0.000 | 0.011 |
| i (IPHAS - APASS) | +0.000 | 0.011 |
| r (IPHAS - SDSS) | -0.001 | 0.029 |
| i (IPHAS - SDSS) | -0.002 | 0.032 |

on one hand, and to avoid sources near the faint detection limit of APASS on the other.

The resulting set of 220,000 cross-matched stars were then used to derive APASS-to-IPHAS magnitude transformations using a linear least-squares fitting routine, which iteratively removed 3σ -outliers to improve the fit. The solution converged to:

$$r_{\text{IPHAS}} = r_{\text{APASS}} - 0.121 + 0.032(r - i)_{\text{APASS}} \quad (3)$$

$$i_{\text{IPHAS}} = i_{\text{APASS}} - 0.364 + 0.006(r - i)_{\text{APASS}} \quad (4)$$

The root mean square (rms) residuals of these transformations are 0.041 and 0.051, respectively. The small colour terms in the equations indicate that the IPHAS and APASS broadband filters are very similar. The transformations include a large fixed offset, but this is simply due to the fact that APASS magnitudes are given in the AB system and IPHAS uses Vega-based magnitudes. Separate transformations were derived for sightlines with varying extinction properties to investigate the robustness of the transformations with respect to different reddening regimes. This sensitivity was found to be insignificant, in keeping with the scarcity of heavily-reddened objects at $r < 16$.

Having transformed APASS magnitudes into the IPHAS system, we then computed the median magnitude offset for each field which contained at least 30 cross-matched stars. This was achieved for 48 per cent of our fields (shown in Figs. 7 and 8). The offsets follow a near-Gaussian distribution with mean and sigma 0.014 ± 0.104 mag in r and 0.007 ± 0.108 mag in i (Table 3). A total of 4,596 IPHAS fields showed a median offset exceeding ± 0.03 mag in either r or i when compared to APASS.

We then applied the most important step in our re-calibration scheme, which is to adjust the provisional zeropoints of these 4,596 aberrant fields such that their offset is

brought to zero. This allowed the mean IPHAS-to-APASS offset to be brought down to 0.000 ± 0.011 mag in both r and i (Table 4). The procedure of fitting magnitude transformations and correcting the IPHAS zeropoints was repeated a few times to ensure convergence, which was closely approached after the first iteration.

4.2.2 Adjusting fields not covered by APASS

At the time of writing, the APASS catalogue did not provide sufficient coverage for 7,359 of our fields. Fortunately, these fields are located mainly at low Galactic longitudes (cf. Figs. 7 and 8), which were typically observed during the summer months when photometric conditions are more prevalent at the telescope. These remaining fields have nevertheless been brought onto the same uniform scale by employing an ubercalibration-style scheme, which minimises the magnitude offsets between stars located in the overlap regions between neighbouring fields.

An algorithm for achieving this minimisation has previously been described by Glazebrook et al. (1994). In brief, there are two fundamental quantities to be minimised between each pair of overlapping exposures, denoted by the indices i and j . First, the mean magnitude difference between stars in the overlap region $\Delta_{ij} = \langle m_i - m_j \rangle = -\Delta_{ji}$ is a local constraint. Second, to ensure the solution does not stray far from the existing calibration, the difference in zeropoints $\Delta ZP_{ij} = -\Delta ZP_{ji}$ between each pair of exposures must also be minimised.

Minimisation of these two quantities is a linear least squares problem because the magnitude m depends linearly on the ZP (Eqn. 11). Hence we can find the ZP shift to be applied to each field by minimising the sum:

$$S = \sum_{i=1}^N \sum_{j=1}^N w_{ij} \theta_{ij} (\Delta_{ij} + a_i - a_j)^2, \quad (5)$$

where i denotes an exposure, j an overlapping exposure, N the number of exposures, a_i the ZP to solve for, and a_j the ZP of an overlapping field ($\Delta ZP_{ij} = a_i - a_j$). w_{ij} are weights set to the inverse square of the uncertainty in Δ_{ij} , and θ_{ij} is an overlap function equal to either 1 if exposures i and j overlap or 0 otherwise. Solving for a_i is equivalent to solving $\partial S / \partial a_i = 0$, which gives the matrix equation:

$$\sum_{j=1}^N A_{ij} a_j = b_j, \quad (6)$$

where

$$A_{ij} = \delta_{ij} \sum_{k=1}^N w_{jk} \theta_{jk} - w_{ij} \theta_{ij}, \quad (7)$$

$$b_i = \sum_{j=1}^N w_{ij} \theta_{ij} \Delta_{ji} = - \sum_{j=1}^N w_{ij} \theta_{ij} \Delta_{ij}. \quad (8)$$

We enforce a strong external constraint on the solution by keeping the zeropoint fixed for the fields which have already been compared and calibrated against APASS. We hereafter refer to these fields as *anchors*. It is asserted that the zeropoints a_i of the anchor fields are known and not solved for. However they do appear in the vector b_j as constraints. In addition to the APASS-based anchors, we selected 3,273 additional anchor fields by hand to provide

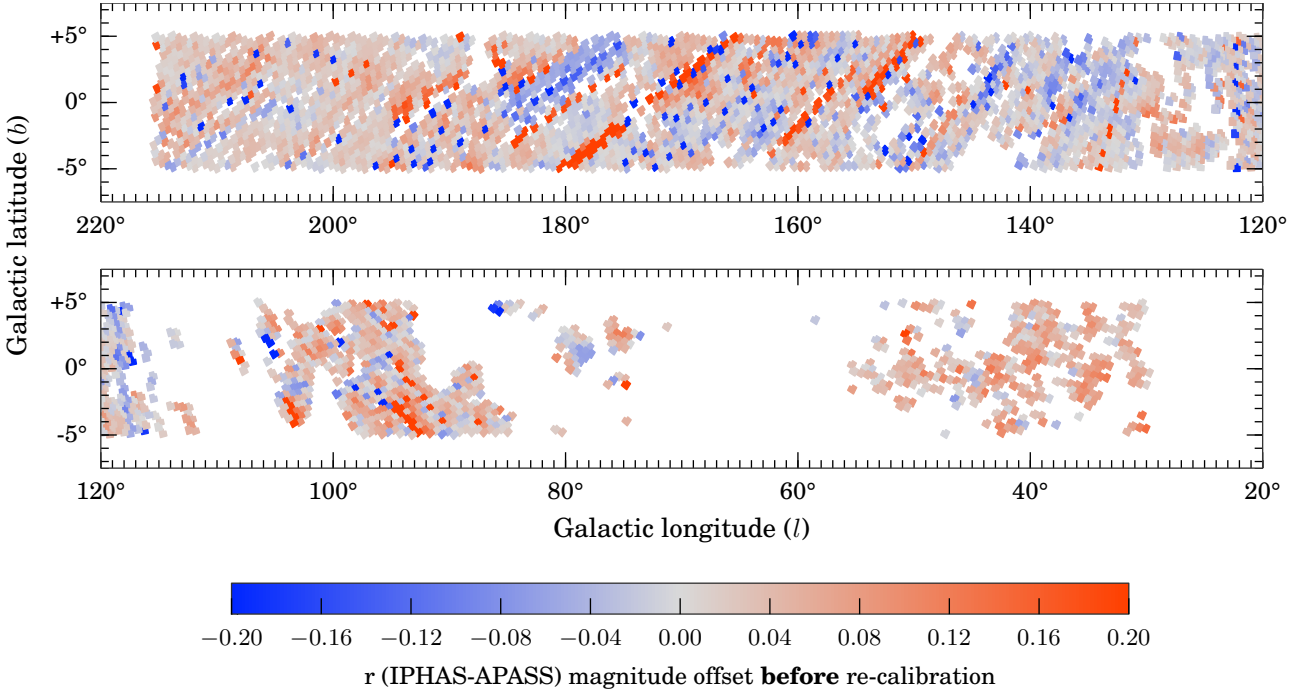


Figure 7. Median magnitude offset in the r band between IPHAS and APASS, plotted on a field-by-field basis prior to the re-calibration procedure. Each square represents the footprint of an IPHAS field which contains at least 30 stars with a counterpart in the APASS DR7 catalogue. The colours denote the median IPHAS-APASS magnitude offset in each field, which was computed after applying the APASS-to-IPHAS transformation to the APASS magnitudes (Eqn. 3). For clarity, we do not show the fields at the offset positions.

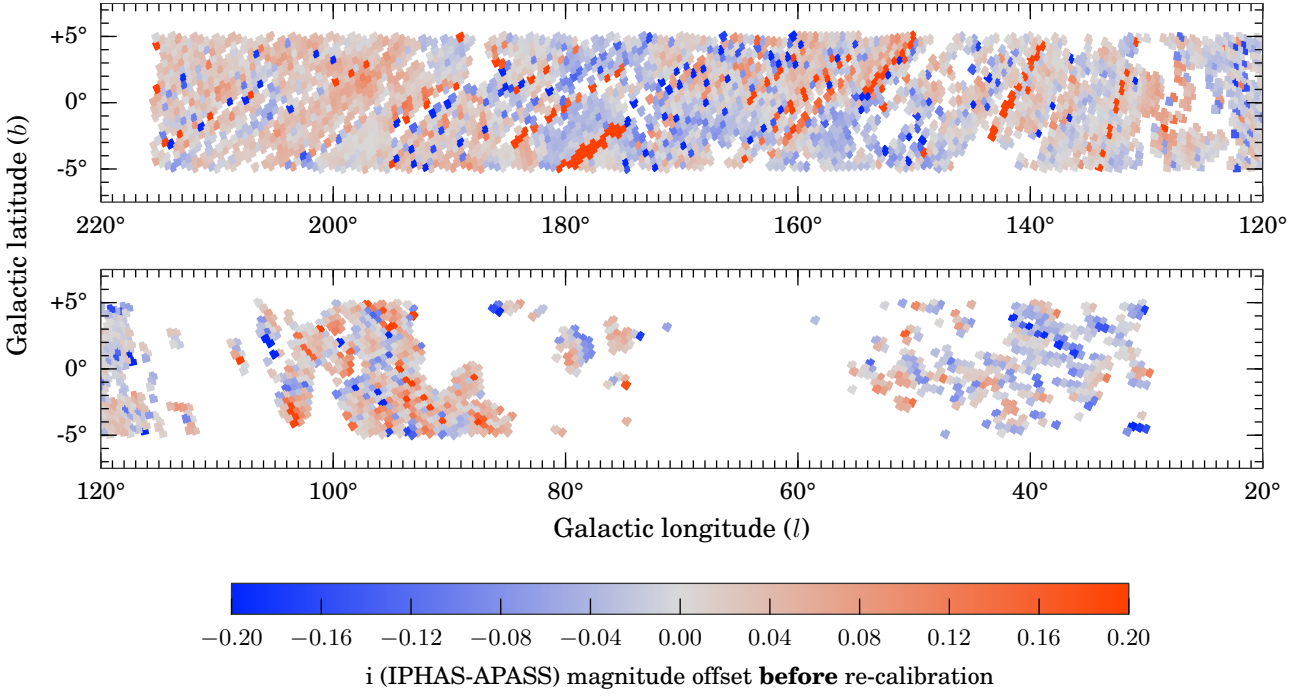


Figure 8. Same as Fig. 7 for the i -band.

additional constraints in regions not covered by APASS. These extra anchors were deemed to have accurate zeropoints based on (i) the information contained in the observing logs, (ii) the stability of the standard star zeropoints during the night, and (iii) photometricity statistics provided by the Carlsberg Meridian Telescope, which is located ~ 500 m from the INT.

We then solved Eqn. 6 for the r and i bands separately using the least-squares routine in Python’s SCIPY.SPARSE module for sparse matrix algebra. This provided us with corrected zeropoints for the remaining fields, which were shifted on average by $+0.02 \pm 0.11$ in r and $+0.01 \pm 0.12$ in i compared to their provisional calibration.

We then turned to the global calibration of the $H\alpha$ data. It is not possible to re-calibrate the narrowband in the same way as the broadbands, because the APASS survey does not offer $H\alpha$ photometry. We can reasonably assume, however, that the corrections required for r and $H\alpha$ are identical, much of the time, because the IPHAS data-taking pattern ensured that a field’s $H\alpha$ and r -band exposures were taken consecutively, albeit separated by a ~ 30 s read-out time. Hence, we have corrected the $H\alpha$ zeropoints by re-using the zeropoint adjustments that were derived for the r band in the earlier steps. An exception was made for 3,101 fields for which our quality-control routines revealed strong zeropoint variations during the night, suggesting non-photometric conditions. In these cases, the $H\alpha$ zeropoints were adjusted by solving Eqn. 6 rather than by simply applying Eqn. 2.

4.3 Testing the calibration against SDSS

Having re-calibrated all fields to the expected APASS accuracy of 3 per cent, we turned to a different survey, SDSS Data Release 9 (Ahn et al. 2012), to validate the results. **SDSS DR9 includes photometry across several strips at low Galactic latitudes, which were observed as part of the Sloan Extension for Galactic Understanding and Exploration (SEGUE; Yanny et al. 2009).** These strips provide data across 18 per cent of the fields in our data release. We cross-matched the IPHAS fields against the subset of objects marked as reliable stars in the SDSS catalogue⁶ in much the same way as for APASS, with the difference of selecting from the fainter magnitude ranges of $15 < r_{\text{SDSS}} < 18.0$ and $14.5 < i_{\text{SDSS}} < 17.5$. This provided us with a set of 1.2 million cross-matched stars.

Colour transformations were again obtained using a sigma-clipped linear least squares fit:

$$r_{\text{IPHAS}} = r_{\text{SDSS}} - 0.093 - 0.044(r - i)_{\text{SDSS}} \quad (9)$$

$$i_{\text{IPHAS}} = i_{\text{SDSS}} - 0.318 - 0.095(r - i)_{\text{SDSS}}. \quad (10)$$

The rms residuals of these transformations are 0.045 and 0.073, respectively. The equations are similar to the ones previously determined for APASS, although the colour terms are slightly larger. The throughput curve of the SDSS i -band filter appears to be somewhat more sensitive at longer wavelengths than both the IPHAS and APASS filters.

⁶ We used the CasJobs facility located at <http://skyserver.sdss3.org/CasJobs> to obtain photometry from the SDSS PHOTOPRIMARY table with criteria $\text{TYPE} = \text{STAR}$, $\text{CLEAN} = 1$ and $\text{SCORE} > 0.7$.

These global transformations were deemed adequate for the purpose of validating our calibration in a statistical sense. Separate equations were derived towards different sightlines to investigate the effects of varying reddening regimes. The colour term was found to show some variation towards weakly reddened areas, where different stellar populations are observed. The vast majority of red objects in the global sample are those in highly reddened areas, however, which agree well with the global transformations and dominate the statistical appraisal of our calibration.

Having transformed SDSS magnitudes into the IPHAS system, we then computed the median magnitude offset for each IPHAS field which contained at least 30 objects with a cross-matched counterpart in SDSS. This was the case for 2,602 fields. The median offsets for each of these fields are shown in Figs. 9 and 10. Importantly, the mean offset and standard deviation found is -0.001 ± 0.029 mag in r and -0.002 ± 0.032 mag in i (Table 4). In comparison, offsets computed in the identical way *before* carrying out the re-calibration showed means of $+0.016 \pm 0.088$ mag in r and $+0.010 \pm 0.089$ mag in i (Table 4). We conclude that our re-calibration procedure has been successful in improving the uniformity of the calibration by a factor three (i.e. from $\sigma = 0.088$ to $\sigma = 0.029$ in r), and as such has achieved our aim of bringing the accuracy to the aimed level of 0.03 mag.

The SDSS comparison revealed a number of fields where the offsets exceeded 0.05 mag (523 fields) or even 0.1 mag (18 fields). This pattern of outliers is consistent with the tails of a Gaussian distribution with $\sigma = 0.03$. Furthermore, it should not be forgotten that both the SDSS and APASS calibrations are approximations to perfection and will not be entirely free of anomalies. Indeed as we worked, we noticed the occasional unsurprising examples of inconsistency between these two surveys.

5 SOURCE CATALOGUE GENERATION

Having obtained a quality-checked and re-calibrated data set, we now turn to the challenge of transforming the observations into a user-friendly catalogue. The aim is to present the best-available information for each unique source in a convenient format, including flags to warn about quality issues such as source blending and saturation. Compiling the catalogue involved four steps:

(i) the single-band detection tables produced by the CASU pipeline were augmented with new columns and warning flags;

(ii) the detection tables were merged into multi-band field catalogues;

(iii) the overlap regions of the field catalogues were cross-matched to flag duplicate (repeat) detections and identify the primary (best) detection of each unique source; and

(iv) these primary detections were compiled into the final source catalogue.

Each of these four steps are explained next.

5.1 User-friendly columns and warning flags

Enhancement of the detection tables by creating new columns is the necessary first step because the tables gener-

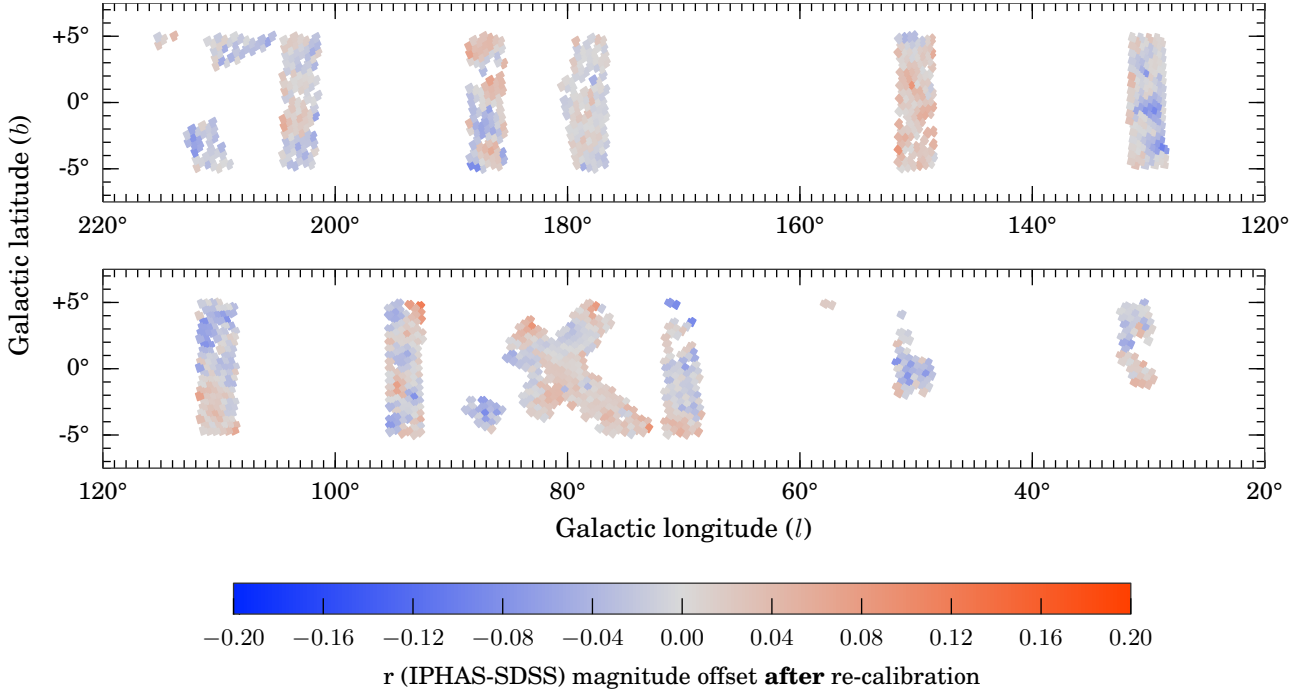


Figure 9. Median magnitude offset between IPHAS and SDSS in the r band *after* the re-calibration procedure using APASS was applied. Each square represents the footprint of an IPHAS field which contains at least 30 stars with a counterpart in the SDSS DR9 catalogue. The colours denote the median IPHAS-SDSS magnitude offset in each field, which was computed after applying the SDSS-to-IPHAS transformation to the SDSS magnitudes (Eqn. 9).

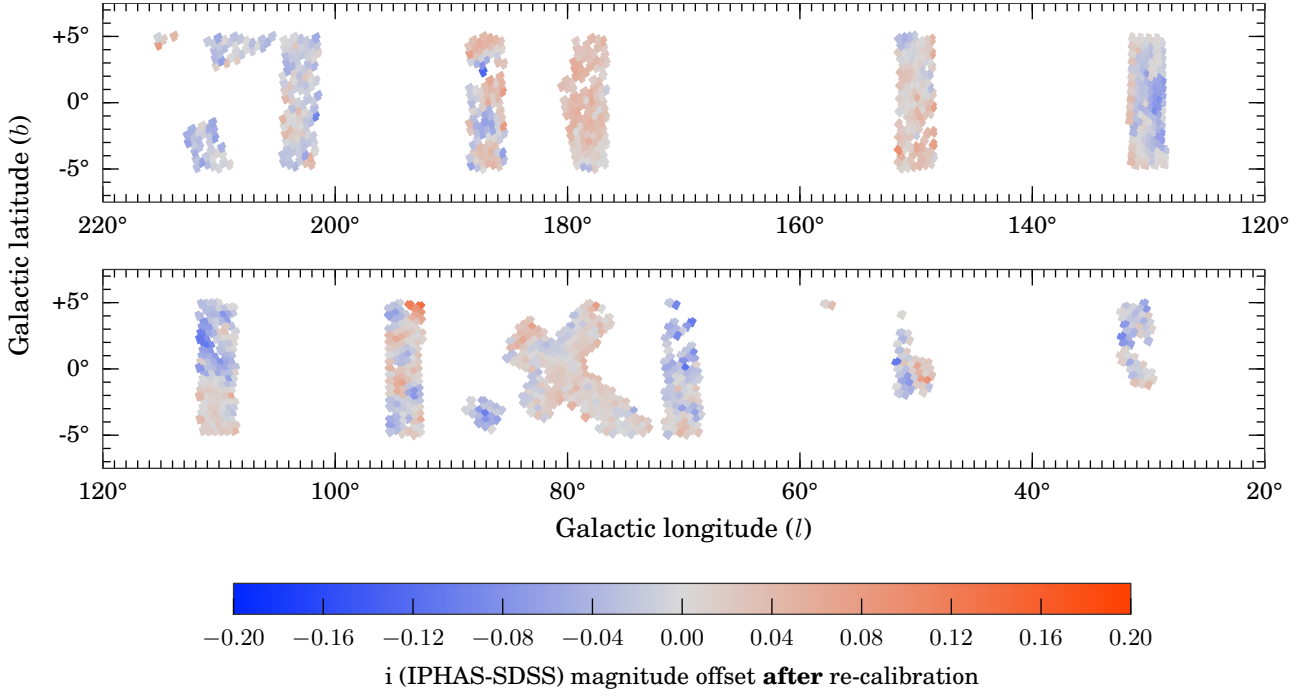


Figure 10. Same as Fig. 9 for the i -band.

ated by the CASU pipeline refer to source positions in pixel coordinates, to photometric measures in number counts, and so on, rather than in common astronomical units. To transform these data into user-friendly quantities, we have largely adopted the units and naming conventions which are in use at the Wide Field Camera (WFCAM) Science Archive (WSA; Hambly et al. 2008) and the Visible and Infrared Survey Telescope for Astronomy (VISTA) Science Archive (VSA; Cross et al. 2012). These archives curate the high-resolution near-infrared photometry from both the United Kingdom Infrared Telescope (UKIRT) Infrared Deep Sky Survey (UKIDSS; Lawrence et al. 2007) and the VISTA Variables in the Via Lactea survey (VVV; Minniti et al. 2010). There is a significant degree of overlap between the footprints of UKIDSS Galactic Plane Survey (GPS; Lucas et al. 2008) and IPHAS, and hence by adopting a similar catalogue format we hope to facilitate scientific applications which combine both data sets.

A detailed description of each column in our source catalogue is given in Appendix A. In the remainder of this section we highlight the main features.

First, we note that each source is uniquely identified by an IAU-style designation of the form ‘IPHAS2 JHH-MMSS.ss+DDMMSS.s’ (cf. column *name* in Appendix A), where ‘IPHAS2’ refers to the present data release and the remainder of the string denotes the J2000 ICRS coordinates in sexagesimal format. For convenience, the coordinates are also included in decimal degrees (columns *ra* and *dec*) and in Galactic coordinates (columns *l* and *b*). We have also included an internal object identifier string of the form ‘#run-#ccd-#detection’ (e.g. ‘64738-3-6473’), which documents the INT exposure number (#run), the CCD number (#ccd), and the row number in the CASU detection table (#detection). These columns are named *rDetectionID*, *iDetectionID*, *haDetectionID*.

Photometry is provided based on the 2.³-arcsec diameter circular aperture by default (columns *r*, *i*, *ha*). The choice of this aperture size as the default is based on a trade-off between concerns about small number statistics and centroiding errors for small apertures on one hand, and diminishing signal-to-noise ratios and source confusion for large apertures on the other hand. The user is not restricted to this choice, because the catalogue also provides magnitudes using three alternatives: the peak pixel height (columns *rPeakMag*, *iPeakMag*, *haPeakMag*), the circular 1.2-arcsec-diameter aperture (*rAperMag1*, *iAperMag1*, *haAperMag1*) and the 3.3-arcsec-diameter aperture (*rAperMag3*, *iAperMag3*, *haAperMag3*).

Each of these magnitude measurements have been corrected for the flux lost outside of the respective apertures, using a correction term which is inferred from the mean shape of the PSF measured locally in the CCD frame. In the case of a point source, the four alternative magnitudes are expected to be consistent with each other to within the photon noise uncertainty (which is given in columns *rErr*, *rPeakMagErr*, *rAperMag1Err*, *rAperMag3Err*, etc). When this is not the case, it is likely that the source is either an extended object for which the aperture correction is invalid, or that the object has been incorrectly measured as a result of source blending or a rapidly spatially-varying nebulous background. In §6.2 we will explain that the consistency of the different-aperture magnitude measurements can be used

as a criterion for selecting stellar objects with accurate photometry.

The brightness of each object as a function of increasing aperture size is also used by the CASU pipeline to provide a discrete star/galaxy⁷/noise classification flag classification flag (*rClass*, *iClass*, *haClass*) and a continuous stellarness-of-profile statistic (*rClassStat*, *iClassStat*, *haClassStat*). For convenience, we have combined these single-band morphological measures into band-merged class probabilities and flags using the merging scheme in use at the WSA⁸ (*pStar*, *pGalaxy*, *pNoise*, *mergedClass*, *mergedClassStat*).

Information on the quality of each detection is included in a series of additional columns. We draw attention to three useful flags which warn about the likely presence of a systematic error:

(i) The *saturated* column is used to flag sources for which the peak pixel height exceeds 55000 counts, which is typically the case for stars brighter than 12-13th magnitude in *r*. Although the pipeline attempts to extrapolate the brightness of saturated stars based on the shape of the PSF, such extrapolation is prone to error, and should be viewed as indicative rather than as precise measurement (systematic uncertainties as a function of magnitude will be discussed in §6.4).

(ii) The *deblend* column is used to flag sources which partially overlap with a nearby neighbour. Although the pipeline applies a deblending procedure to such objects, the procedure is currently applied separately in each band, and hence the (*r* - *i*) and (*r* - $H\alpha$) colours may be inaccurate if the deblending proceeded differently in each band.

(iii) The *brightNeighb* column is used to flag sources which are located within a radius of 5 arcmin from an object brighter than *V* = 7 according to the Bright Star Catalogue (BSC; Hoffleit et al. 1991), or within 10 arcmin if the neighbour is brighter than *V* = 4. These brightest stars are known to cause systematic errors and spurious detections as a result of stray light and diffraction spikes.

In addition to the above, we also created warning flags for internal bookkeeping. For example, we flagged detections which fell in the strongly vignetted regions of the focal plane, which were truncated by CCD edges, or which were otherwise affected by bad pixels in the detector. No such detections have had to be included in the catalogue, as alternative detections were available in essentially all these situations thanks to the IPHAS field pair strategy. Hence there has been no need to include these internal warning flags in the published source catalogue.

Finally, we note that basic information on the observing conditions is included (*fieldID*, *fieldGrade*, *night*, *seeing*). A table containing more detailed quality control information, indexed by *fieldID*, is made available on our website.

⁷ For consistency with the terminology that is used in the CASU pipeline and the WSA/VSA archives, extended objects are classified as ‘galaxies’. This class will flag any type of resolved object, however.

⁸ Explained at [#gpssource_mergedclass](http://surveys.roe.ac.uk/wsa/www/gloss_m.html)

5.2 Band-merging the detection tables

The second step in compiling the source catalogue is to merge the contemporaneous trios of r , i , $H\alpha$ detection tables into multi-band field catalogues. This required a position matching procedure to link sources between the three bands. We used the TMATCHN function of the STILTS software for this purpose, which allows rows from multiple tables to be matched (Taylor 2006). In brief, the algorithm identifies groups of linked detections such that (i) each detection is located within a specified maximum distance from one or more members of the group, (ii) each detection appears in exactly one group, and (iii) the largest possible groups are preferred (i.e. preferably containing three detections from all three bands). The result of the procedure is a band-merged catalogue in which each row corresponds to a group of linked r , i , and $H\alpha$ detections which satisfy the matching distance criterion in a pair-wise sense. Sources for which no counterpart was identified in all three bands are retained in the catalogue as single- or double-band detections, with empty columns for the missing bands.

We employed a maximum matching distance of 1 arcsec, trading off completeness against reliability. On the one hand, a matching distance larger than 1 arcsec was found to allow too many spurious and unrelated sources to be linked. On the other, a value smaller than 1 arcsec would pose problems for very faint sources with large centroiding errors, and would occasionally fail near CCD corners, where the astrometric solution can show local systematic errors which exceed 0.5 arcsec. The position offsets between the r detection and detections in i , and/or $H\alpha$ have been included in the catalogue, giving the user the option to tighten them further if necessary (columns iXi , $iEta$, $haXi$, $haEta$), or simply to examine light centre differences. We note that UKIDSS/GPS adopted the same maximum matching distance for similar reasons (Hambly et al. 2008).

The resulting band-merged catalogues were inspected by eye as part of our quality control procedures and were found to be reliable for the vast majority of objects. We do warn that blended objects can occasionally fall victim to source confusion during the band-merging procedure, which is a complicated problem that we have not attempted to resolve in this release. It is important to bear this in mind when appraising stars of seemingly unusual colours (such as candidate emission line stars). If blending is flagged, or if the inter-band matching distance is unusually large, then the probability that the unusual colour is spurious due to source confusion is greatly increased.

5.3 Selecting the primary detections

We explained earlier that the survey contains repeat observations of identical sources as a result of field offsetting and overlaps. Amongst all sources in the magnitude range $13 < r < 19$, we find that 65 per cent were detected twice

and 25 per cent were detected three times or more. Only 9 per cent were detected once.

Since the principal aim of this data release is to provide accurate photometry at a single epoch, we have focused on providing the magnitudes and coordinates from the *best-available* detection of each object – hereafter referred to as the *primary* detection. Although overlapping fields could have been co-added to gain a small improvement in depth, we have decided against this for two reasons. Firstly, combining the information from multiple epochs would make the photometry of variable stars difficult to interpret. Secondly, co-adding would cause the image quality to degrade towards the mean, which is particularly a drawback for crowded fields.

Anyone interested in the alternative detections of a source – hereafter called the *secondary* detections – can nevertheless obtain this information in two ways. To begin with, whenever a secondary detection was collected within 10 minutes of the primary, we have included the identifier and the photometry of that secondary detection in the catalogue for convenience (columns $sourceID2$, $fieldID2$, $r2$, $i2$, $ha2$, $rErr2$, $iErr2$, $haErr2$, $errBits2$). Second, images not included in the catalogue are made available on our website.

Primary detections have been selected from all available detections using a so-called *seaming* procedure, which we adapted from the algorithm developed for the WSA⁹. In brief, the first step is to identify all the duplicate detections by cross-matching the overlap regions of all field catalogues, again using a maximum matching distance of 1 arcsec. The duplicate detections for each unique source are then ranked according to (i) filter coverage, (ii) quality score, and (iii) the average seeing of stars in the CCD frame rounded to 0.2 arcsec. If this ranking scheme reveals multiple ‘winners’ of seemingly identical quality, then the one that was observed closest to the optical axis of the camera is chosen.

5.4 Compiling the final source catalogue

As the final step, the primary detections selected above were compiled into the final 99-column source catalogue that is described in Appendix A. The original unweeded list of sources naturally included a significant number of spurious entries as a result of the sensitive detection level that is employed by the CASU pipeline. We have decided to enforce three basic criteria which must be met for a candidate source to be included in the catalogue:

- (i) the source must have been detected at $S/N > 5$ in at least one of the bands, i.e. it is required that at least one of $rErr$, $iErr$ or $haErr$ is smaller than 0.2 mag;
- (ii) the shape of the source must not be an obvious cosmic ray or noise artefact, i.e. we require either $pStar$ or $pGalaxy$ to be greater than 20 per cent;
- (iii) the source must not have been detected in one of the strongly vignetted corners of the detector, not have had any known bad pixels in the aperture, and not have been on the edge of one of the CCDs.

⁹ <http://surveys.roe.ac.uk/wsa/dboverview.html#merge>

Table 5. Breakdown of catalogue sources as a function of the band(s) in which the object was detected. We also show the fraction of ‘confirmed’ sources, which we define as those objects detected in more than one field (usually the field pair partner).

| Band(s) | Sources [10^6] | Confirmed ($nObs > 1$) |
|-----------------|-----------------------|-----------------------------|
| $r, i, H\alpha$ | 159 | 91% |
| r, i | 25 | 77% |
| $i, H\alpha$ | 3 | 73% |
| $r, H\alpha$ | 2 | 65% |
| i | 15 | 43% |
| r | 9 | 27% |
| $H\alpha$ | 6 | 12% |
| Total | 219 | 81% |

A total of 219 million primary detections satisfied the above criteria and have been included in the catalogue.

Table 5 details the breakdown of these sources as a function of the bands in which they are captured. 159 million sources are detected in all three filters (73 per cent), 30 million are detected in two filters (14 per cent), and the remaining 30 million are single-band detections. Table 5 also presents the fraction of ‘confirmed’ objects, which we define as those sources which have been detected more than once (recall that much of the survey area is observed twice due to the field pair strategy). We find that the single-band detections tend to show much lower confirmation rates (32 per cent on average) than double- and triple-band detections (89 per cent). This suggests that a significant fraction of these entries may be spurious detections.

Not all the single-band detections are spurious, however. We note that the confirmation rate for i -band detections is markedly better than for r and $H\alpha$, which is likely explained by the fact that i is least affected by interstellar extinction, and so the survey can occasionally pick up highly-reddened objects in i which are otherwise lost in r and $H\alpha$. Moreover, objects which are intrinsically very red may also be picked up in i alone, while faint objects with very strong Balmer emission may appear only in $H\alpha$. Nevertheless, we recommend users not to rely on single-band objects without inspecting the image data by eye, or verifying that the object was detected more than once ($nObs > 1$).

6 DISCUSSION

We now offer an overview of the properties of the catalogue by discussing (i) the known caveats, (ii) the recommended quality criteria, (iii) the reliability of sources, (iv) the photometric uncertainties, and (v) the source densities.

6.1 Known caveats

Like any other photometric survey which operates close to the detection and resolution limits, our catalogue inevitably contains sources with are spurious

or have been parametrised inaccurately. In what follows, we highlight the most common caveats which users of the catalogue might face, followed by a discussion on how they can be avoided. Known caveats include:

- *Spurious objects.* Nebulous sky backgrounds, saturation artefacts near bright stars, and cosmic rays are known to be able to trigger spurious detections. The majority of these can be removed by requiring that a detection is made in more than one band ($nBands > 1$), on more than one occasion ($nObs > 1$), or by ensuring that the object looks like a perfect point source ($pStar > 0.9$).

- *Source blending and confusion.* Blended objects are known to be parametrised less accurately and to be more prone to source confusion during the band-merging procedure. We remind the reader that such objects are flagged in the catalogue using the columns $rDeblend$, $iDeblend$, $haDeblend$, and $deblend$.

- *Low S/N detections.* The majority of the objects in our catalogue are faint sources observed near the detection limits, e.g. 55 per cent of the entries in the catalogue are fainter than $r > 20$. The measurements of faint objects are naturally prone to larger random and systematic uncertainties: for example, an inaccurately-subtracted background will introduce a proportionally larger systematic error for a faint object. These objects can be removed by ensuring that an object is detected at $S/N > 10$ and has photometry which is consistent across the different aperture sizes. Such objects are flagged in the catalogue using the $a10$ column.

- *Saturation.* The photometry and astrometry of objects brighter than the saturation limit of the instrument is subject to systematic errors. Such objects can be removed by ensuring that the columns $rSaturated$, $iSaturated$, $haSaturated$ or $saturated$ are set to “False”.

We note that it is not possible, at this stage, to include an exhaustive list of all the caveats, because we cannot anticipate all forms of use of the data. For this reason, we recommend users to read the FAQ section on our website, which will be updated as user experience accumulates.

6.2 Recommended quality criteria

Most applications will require a combination of quality criteria to be used to avoid the caveats outlined above. The choice of criteria will always tension completeness against reliability, i.e. the fraction of spurious sources. To aid users we have listed two sets of recommended quality criteria in Tables 6 and 7.

First, Table 6 specifies a set of minimum quality criteria which should benefit most applications which desire accurate colours as well as completeness down to ~ 19 th magnitude. The listed criteria are designed to (i) remove low-S/N sources, (ii) remove saturated objects, and (iii) remove sources for which the $2''3$ -diameter aperture magnitude is

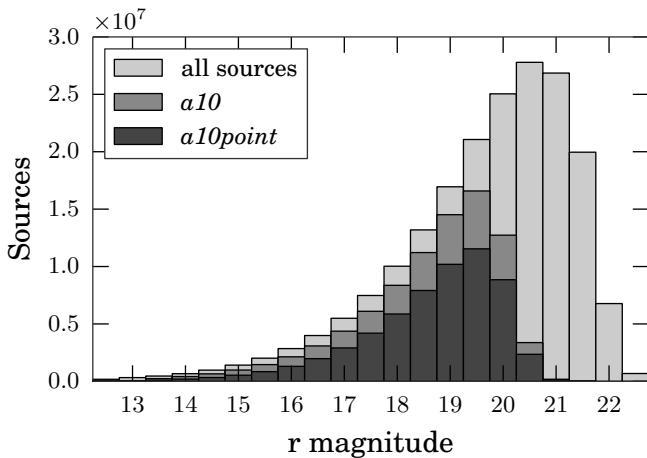


Figure 11. r-band magnitude distribution for all objects in the catalogue (light grey). Overlaid we also show the distribution for objects detected at $S/N > 10$ in all bands selected according to the quality criteria described in Table 6 (*a10*, grey), and for the set of unconfused 10σ point source detections described in Table 7 (*a10point*, dark grey). The distributions for *i* and $H\alpha$ look identical, apart from being shifted by about 1 and 0.5 mag towards brighter magnitudes, respectively.

inconsistent with its alternative 1.^{''}2-diameter measurement. This latter criterion is a proxy for identifying objects which are affected by poor background subtraction or failed deblending. A total of 86 million sources out of 219 million (39 per cent) satisfy all the criteria listed in Table 6 and are hereafter referred to as ‘*a10*’. For convenience, the catalogue contains a boolean column named *a10* that flags these objects.

For applications which require a higher standard of accuracy at the expense of completeness, a set of additional quality criteria are suggested in Table 7. These criteria are designed to ensure that (i) the object appeared as a perfect point source, (ii) the object was not blended with a nearby neighbour, and (iii) the object was not located near a very bright star. 59 million sources (27 per cent) satisfy these stricter criteria and are hereafter referred to as ‘*a10point*’. Again, the catalogue contains a boolean column named *a10point* which flags these objects.

Fig. 11 compares the *r*-band magnitude distributions for objects tagged *a10* and *a10point* against the unfiltered catalogue. In the magnitude range $13 < r < 19$, we find that 81 per cent of the sources are flagged *a10* and 54 per cent are flagged *a10point*. We will explain below that the *a10point* category is least complete at low Galactic longitudes, where source blending can affect up to a quarter of the objects.

It is easy to see how the quality criteria may be adapted to be more tolerant. For example, by raising the allowed photometric uncertainties from 0.1 mag to 0.2 mag in Table 6, 42 million candidate sources would be added to the 109 million satisfying the tighter error bound. Our choice to adopt 0.1 mag as the cut-off uncertainty for the *a10* category is a

pragmatic trade-off which we found to suit many science applications, but users are encouraged to revise the quality criteria according to their needs.

6.3 Source reliability

Having obtained a set of quality criteria, we now assess how these improve the data quality. In this section we start by discussing the *reliability* of the survey, which we define as the fraction of sources which are genuine astrophysical objects. To estimate the reliability, we cross-matched IPHAS against SDSS DR7¹⁰, which is a catalogue of similar resolution and depth. By computing the fraction of IPHAS sources which were also independently detected by SDSS, we can obtain a good lower limit on the reliability.

The comparison was carried out across three cone-shaped regions, each covering 1 deg², using a strict cross-matching distance of 0.5 arcsec. We considered four subsets of the IPHAS catalogue:

- (i) the entire (unfiltered) catalogue;
- (ii) objects detected in all three bands;
- (iii) *a10* sources;
- (iv) *a10point* sources.

The results for each of the regions and subsets are presented in Table 8. We find that our catalogue shows a good baseline reliability (90.8 per cent), which is improved markedly by the simple requirement that a source needs to be detected in all three bands (98.7 per cent). Reliabilities of 99.5 and 99.7 per cent are achieved using the *a10* and *a10point* quality flags.

To understand the nature of the small fraction of *a10point*-flagged sources which appear to be unreliable in this test, we investigated the data by eye. We found these ‘unreliable’ objects to be located in the vicinity of moderately bright stars ($r \lesssim 12$), tracing out an area which is affected by saturation spikes or scattered light in the SDSS images. In all cases we found these remaining objects to appear as genuine stars in both the IPHAS and SDSS images. It is hence likely that the reliability of the *a10point* class is close to 100 per cent.

6.4 Random and systematic uncertainties

Fig. 12 shows the mean photometric uncertainties ($rErr$, $iErr$, $haErr$) as a function of magnitude. We find the typical uncertainty to reach 0.1 mag near $r = 20.5$ and $i, H\alpha = 19.5$. We note that the fainter depth in *r* is compensated by the fact that most stars have brighter magnitudes in *i* and $H\alpha$; the average colours in the catalogue are $\langle r - i \rangle = 1.06 \pm 0.12$ and $\langle r - H\alpha \rangle = 0.44 \pm 0.03$. We warn that the statistics

¹⁰ SDSS DR7 was chosen for this comparison due to an apparent change in the catalogue generation for DR8 and DR9, which resulted in fewer genuine stars being detected near bright ($r < 12$) sources, which in turn gave an unduly pessimistic view on our reliability.

Table 6. Recommended quality criteria for selecting objects with accurate colours. These criteria serve to identify objects detected at $S/N > 10$ in all three bands without being saturated, and with the added requirement that the photometric measurements need to be consistent across different aperture sizes. The 86 million objects which satisfy these criteria have been flagged in the catalogue using the column named *a10* (short for “all-band 10σ ”).

| Quality criterion | Rows passed | Description |
|--|-------------------|--|
| $rErr < 0.1 \text{ AND } iErr < 0.1 \text{ AND } haErr < 0.1$ | 109 million (50%) | Require the photon noise to be less than 0.1 mag in all bands (i.e. $S/N > 10$). This implicitly requires a detection in all three bands. |
| NOT <i>saturated</i> | 158 million (72%) | The brightness must not exceed the nominal saturation limits. |
| $ r - rAperMag1 < 3\sqrt{rErr^2 + rAperMag1Err^2} + 0.03$ | 176 million (80%) | Require the <i>r</i> magnitude measured in the default $2''.3$ -diameter aperture to be consistent with the measurement made in the smaller $1''.2$ aperture, albeit tolerating a 0.03 mag systematic error. This will reject sources for which the background subtraction or the deblending procedure was not performed reliably. |
| $ i - iAperMag1 < 3\sqrt{iErr^2 + iAperMag1Err^2} + 0.03$ | 183 million (84%) | Same as above for <i>i</i> . |
| $ ha - haAperMag1 < 3\sqrt{haErr^2 + haAperMag1Err^2} + 0.03$ | 158 million (72%) | Same as above for Ha. |
| All of the above (flagged as <i>a10</i>) | 86 million (39%) | |

Table 7. Additional quality criteria which are recommended for applications which require objects to be single, unconfused point sources with accurate colours. The 59 million sources which satisfy these criteria have been flagged using the column named *a10point*.

| Quality criterion | Rows passed | Description |
|--|-------------------|--|
| <i>a10</i> | 86 million (39%) | The object must satisfy the criteria for accurate colours listed in Table 6. |
| <i>pStar</i> > 0.9 | 145 million (66%) | The object must appear as a perfect point source, as inferred from comparing its PSF with the average PSF measured in the same CCD. |
| NOT <i>deblend</i> | 177 million (81%) | The source must appear as a single, unconfused object. |
| NOT <i>brightNeighb</i> | 216 million (99%) | There is no star brighter than $V < 4$ within $10'$, or brighter than $V < 7$ within $5'$. Such very bright stars cause scattered light and diffraction spikes, which may add systematic errors to the photometry or even trigger spurious detections. |
| All of the above (flagged as <i>a10point</i>) | 59 million (27%) | |

Table 8. Fractions of sources in our catalogue which are also found in the SDSS DR7 catalogue within a cross-matching radius of 0.5 arcsec. These statistics can be interpreted as lower limits for the reliability of our sources, i.e. the probability that an entry in our catalogue is a genuine astrophysical source rather than an instrumental artefact. The fractions were computed in three 1 deg² regions where both surveys show contiguous overlap. The reliability is shown for IPHAS sources without selection criteria applied (“all”), using only objects detected in all three bands ($nBands = 3$), using objects detected at 10σ in all three bands ($a10$), and finally using the detections classified as reliable 10σ point sources ($a10point$).

| Region (ℓ, b) | all | $nBands = 3$ | $a10$ | $a10point$ |
|----------------------|-------|--------------|-------|------------|
| (149.39, 4.06) | 93.0% | 98.8% | 99.7% | 99.8% |
| (186.59, -2.50) | 90.0% | 98.8% | 99.4% | 99.6% |
| (202.70, -1.75) | 89.4% | 98.5% | 99.4% | 99.7% |
| mean | 90.8% | 98.7% | 99.5% | 99.7% |

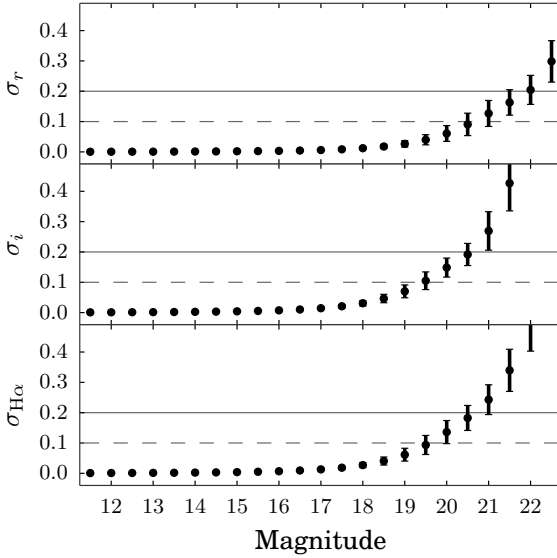


Figure 12. Mean photometric uncertainties for r (top), i (middle) and $H\alpha$ (bottom). Data points shown are the average values of columns $rErr$, $iErr$ and $haErr$ in the catalogue, and the error-bars show the standard deviations. The dashed and solid lines indicate the 10σ and 5σ limits, respectively. These statistics show the average level of the Poissonian photon noise and do not include systematic uncertainties.

shown in Fig. 12 are the random errors based on the expected Poissonian photon noise. Systematics, such as calibration and deblending errors, are not included.

To appraise the level at which our photometry is affected by such systematics, we can exploit the secondary measurements which are present in the catalogue (i.e. r vs $r2$, i vs $i2$, ha vs $ha2$). In Fig. 13a we show the mean absolute residuals between these primary and secondary magnitudes as a function of magnitude (black dots). We also plot the Poissonian uncertainties for comparison (solid red line). We find the mean residual and standard deviation to be 0.03 ± 0.04 mag across the magnitude ranges 13 to 18 (r)

and 12 to 17 (i , $H\alpha$), which is consistent with the accuracy of the calibration. Stars fainter than this range appear to be dominated by photon noise (red line), while stars at the bright end appear to suffer from large systematic errors due to saturation effects.

In Fig. 13b we show a similar comparison between the primary and secondary detections, but this time we have only included sources which are flagged as $a10point$ in the catalogue. We do not observe an improvement in the average residuals as a function of magnitude, but the number of outliers has decreased markedly (evidenced by the shorter error bars which denote the standard deviation of the absolute residuals). We conclude that the $a10point$ quality criteria are effective at reducing the level of the systematic errors, while also removing the inaccurate data at the bright and faint end.

6.5 Source counts and blending

Fig. 14 shows the number of sources in the catalogue counted in 1°-wide strips as a function of Galactic longitude (thick blue line). Unsurprisingly, we find the number of sources to increase towards the Galactic centre. For example, the average source density near $\ell \simeq 30^\circ$ is roughly 300,000 objects per square degree, which is six times more than the density found near $\ell \simeq 180^\circ$. In addition to the global trend, variations are also apparent on smaller scales. For example, we find a significant drop near the constellations of Aquila ($\ell \simeq 40^\circ$) and Cygnus ($\ell \simeq 80^\circ$ and $\ell \simeq 90^\circ$), which are regions known to be affected by high levels of foreground extinction (the extremities of ‘the Great Rift’, e.g. Bok & Bok 1941). However, we warn that the source counts shown have not been corrected for field pairs that have yet to be released or for variations in the depth across the included fields. For example, the dip near $\ell \simeq 140^\circ$ is an artificial feature caused by gaps in the footprint coverage (seen in Fig. 2).

In a forthcoming paper, properly-calibrated detailed maps of stellar density of the northern Galactic Plane will be presented (Farnhill et al., in preparation). This will incorporate completeness corrections based on the statistics of artificial source recovery. Such maps are of interest as tests of Galactic models.

Fig. 14 also shows the number counts for non-blended sources (thin red line). These are sources for which the *deblend* flag is FALSE, i.e. sources for which the CASU pipeline did not have to apply a deblending procedure to separate the flux originating from two or more overlapping objects. This provides some insight into how the fraction of blend-affected sources correlates with the local source density. In headline numbers, only 11 per cent of the sources are blended at $\ell > 90^\circ$, whereas 24 per cent are blended at $\ell < 90^\circ$.

Finally, we warn that blended objects are more likely than unblended objects to have fallen victim to source confusion during the band-merging procedure. It is important to bear this in mind when appraising stars of seemingly unusual colours (such as candidate emission line stars) – if blending is flagged, the probability that the unusual colour is spurious is greatly increased.

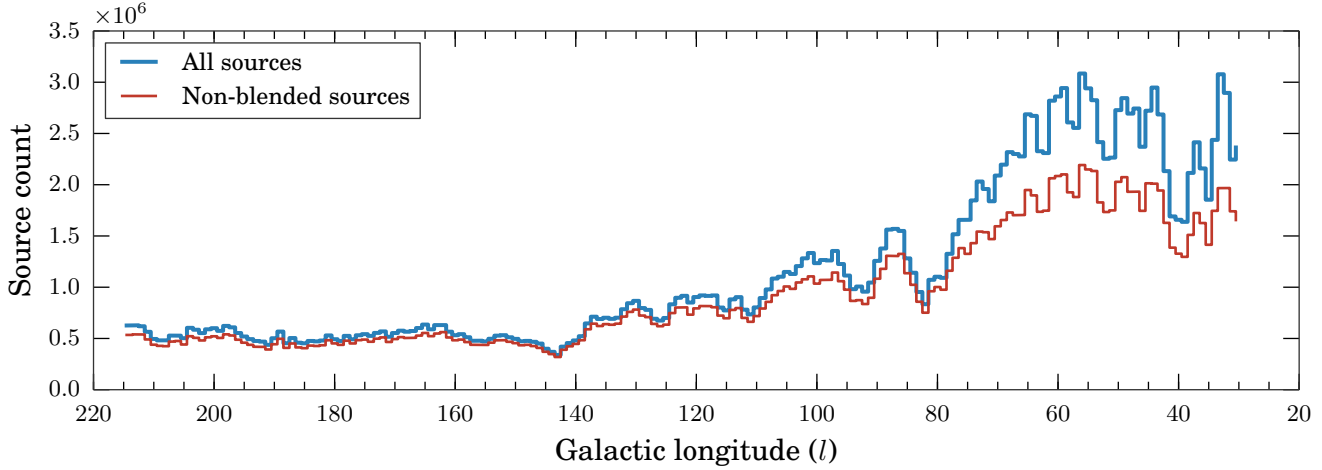


Figure 14. Number of entries in the IPHAS DR2 source catalogue as a function of Galactic longitude. The upper blue line shows the number of sources counted in 1° -wide longitude bins. The lower red line uses the same binning but includes only those sources for which the *deblend* flag is FALSE, i.e. unconfused sources for which the CASU pipeline did not have to apply a deblending procedure. In both cases we counted only those sources in the latitude range $-5^\circ < b < +5^\circ$, such that one may obtain a rough guide to source density by dividing the counts by 10 deg^2 . The global variations in the source counts traces the structure of the Galaxy and the distribution of foreground extinction, but is also affected by instrumental effects such as variations in the observed depth and completeness (see text).

7 DEMONSTRATION

We conclude this paper by demonstrating how the unique $(r - \text{H}\alpha, r - i)$ colour-colour diagram offered by this catalogue can readily be used to (i) characterise the extinction regime along different sightlines, and (ii) identify $\text{H}\alpha$ emission-line objects.

7.1 Colour-colour and colour-magnitude diagrams

The survey's unique $(r - \text{H}\alpha)$ colour, when combined with $(r - i)$, has been shown to provide simultaneous constraints on intrinsic stellar colour and interstellar extinction (Drew et al. 2008). Put differently, the main sequence in the $(r - \text{H}\alpha, r - i)$ diagram runs in a direction that is at a large angle relative to the reddening vector, because the $(r - \text{H}\alpha)$ colour tends to act as a coarse proxy for spectral type and is less sensitive to reddening than $(r - i)$. As a result, the distribution of a stellar population in the IPHAS colour-colour diagram can offer a handle on the properties of the population and the extinction along a line of sight.

This is demonstrated in Fig. 15, 16 & 17, where we present three sets of IPHAS colour/magnitude diagrams towards three distinct sightlines located at Galactic longitudes 180° , 45° and 30° , respectively, which were chosen because they show stellar populations with different characteristics. Each figure contains all the sources flagged as *a10point* within a region of one square degree centred on the coordinates indicated in the diagram (i.e. within a radius of $0^\circ 564$ from the indicated sightline). For clarity, we have imposed the additional criterion that the photometric uncertainties must be smaller than 0.05 mag in each band, corresponding to a cut-off near 19th magnitude.

Each of the diagrams reveals a well-defined locus, which helps to further demonstrate the health of the catalogue

and the global calibration for investigating stellar populations across wide areas. We have annotated the colour-colour diagrams by showing the position of the unreddened main sequence (thin solid line), the unreddened giant branch (thick solid line), and the reddening track for an A0V-type star (dashed line) – all three are based on the Pickles (1998) library of empirical spectra synthesised into the Vega-based IPHAS system by Drew et al. (2005). In the colour-magnitude diagrams we only show the reddening vector together with the unreddened 1 Gyr isochrone due to Bressan et al. (2012), which is made available for the IPHAS system through the on-line tool hosted at the Observatory of Padova (<http://stev.oapd.inaf.it/cmd>). The isochrone and reddening vector have been placed at an arbitrary distance of 2 kpc.

Each of the sightlines reveals a stellar population with distinct characteristics. Towards the Galactic anti-centre at $\ell = 180^\circ$ (Fig. 15) we find a population dominated by lowly-reddened main sequence stars. This is consistent with the estimated total sightline extinction of $E(B - V) = 0.49$ given by Schlegel et al. (1998), and applying the 14 per cent reduction recommended by Schlafly & Finkbeiner (2011). Looking in more detail we can see that the stellar locus is narrower for M-type dwarfs than for earlier types: we do not observe M dwarfs experiencing the strongest reddening possible for this sightline. This implies that extinction is still increasing at distances of $\sim 1\text{-}2$ kpc, where M dwarfs become too faint to be contained in the IPHAS catalogue. It is also clear that there are no unreddened stars earlier than $\sim \text{K}0$ visible; such stars would be saturated if within a few hundred parsecs. This therefore suggests that there is a measurable increase in extinction locally. We also note a relative absence of late type giants which, due to the relative brevity of the corresponding phase of stellar evolution, would only account for a

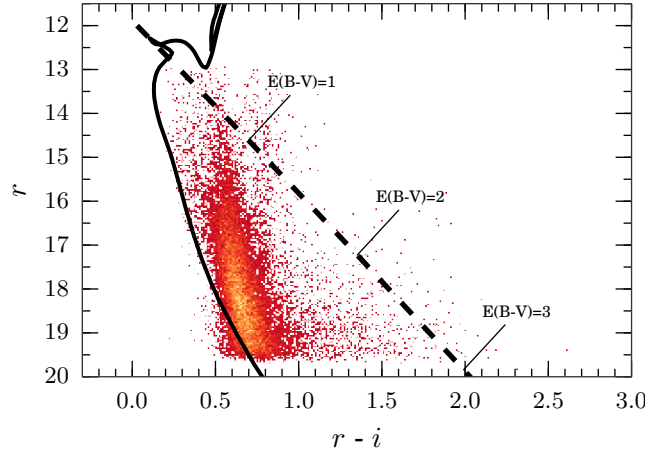
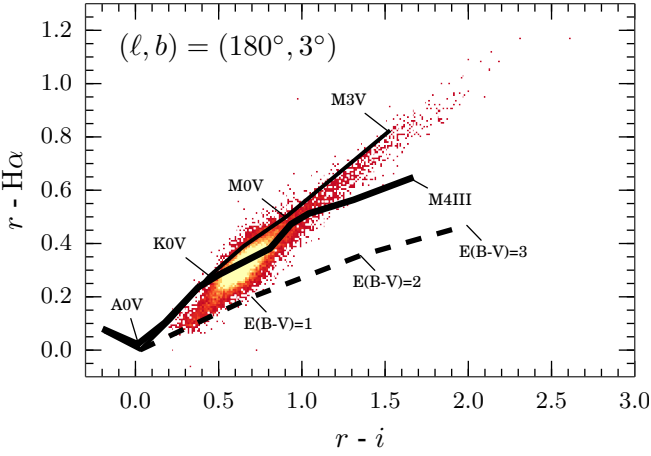


Figure 15. Colour-colour and colour-magnitude diagrams (left and right panel) showing sources flagged as *a10point* located in an area of 1 deg^2 centred near the Galactic anti-centre at $(l, b) = (180^\circ, +3^\circ)$. The diagrams are plotted as 2D-histograms which show the density of objects in bins of 0.01-by-0.01 mag; bins containing 1 to 10 objects are coloured red, while bins with more than 20 objects are yellow. The left panel is annotated with the position of the main sequence (thin solid line), giant stars (thick solid line) and the reddening track for an A0V-type star (dashed line). The right panel shows the unreddened 1 Gyr isochrone from the models by Bressan et al. (2012, solid line) along with the reddening vector for an A0V-type (dashed line), both placed at an arbitrary distance of 2 kpc. This is one of the least reddened sightlines in the survey and hence the observed stellar population appears to be dominated by lowly reddened main sequence stars (see text).

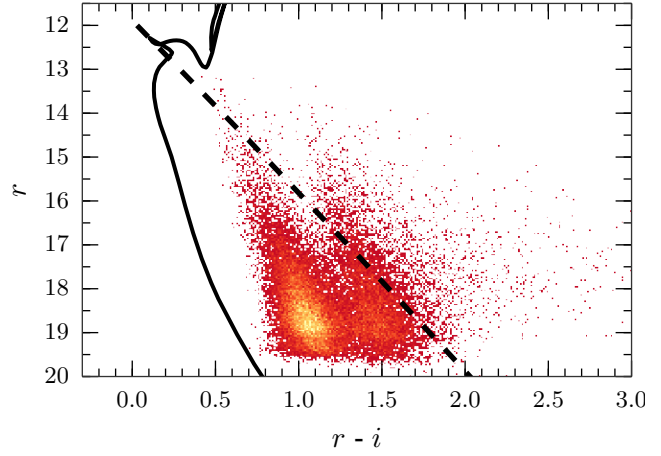
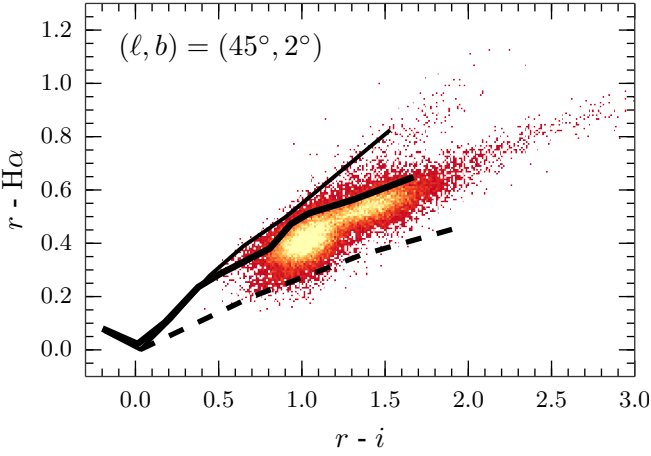


Figure 16. Same as above for $(l, b) = (45^\circ, +2^\circ)$, which is one of the highest-density sightlines in the survey, revealing two groups of stars in colour-magnitude space.

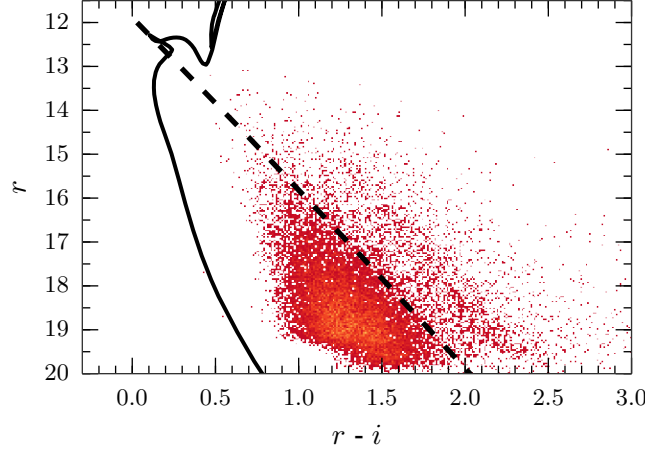
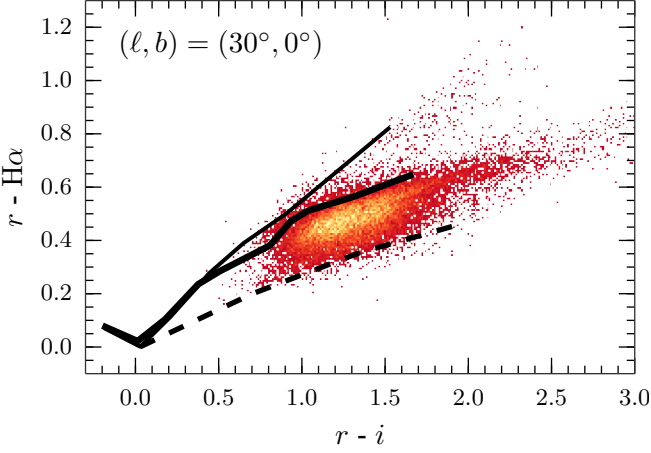


Figure 17. Same as above for $(l, b) = (30^\circ, 0^\circ)$, showing one of the most reddened sightlines in the survey.

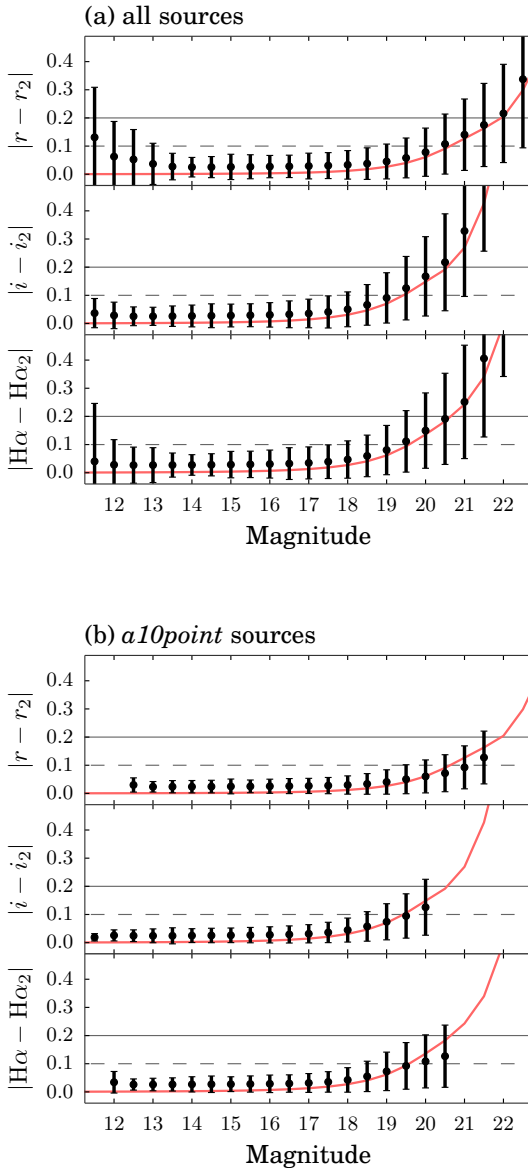


Figure 13. Photometric repeatability as a function of magnitude for all sources in the catalogue (panel a) and for the *a10point* sources alone (panel b). Black dots show the mean absolute residuals between the primary and the secondary detections. The error-bars show the standard deviations. The red trend line shows the average Poissonian uncertainties we derived in Fig. 12. We find that the *a10point* quality criteria are successful at removing objects with large residuals.

small proportion of this more nearly *volume-limited* sample seen in the Anticentre direction.

In contrast, lines of sight passing into the first Galactic quadrant yield samples that are more commonly *magnitude-limited* instead. For example, at $\ell = 45^\circ$ (Fig. 16), there is a wealth of reddened objects and late type giants. In the colour-magnitude diagram, it is clear that the stars are split into two distinct groups, with one significantly redder than the other. The bluer group is composed of main sequence stars, with the slope of this group in the colour-magnitude

diagram attributable to the significantly increasing extinction. Meanwhile the redder group is principally composed of red giant stars (see Wright et al. 2008). As these stars are intrinsically brighter, they will be substantially further away than their main sequence counterparts at the same apparent magnitude. Given that extinction continues to increase with distance, along this sightline, the red giants we observe will be subject to appreciably more reddening than the main sequence stars, pushing them to $(r - i) \sim 1.5$.

Finally, in one of our lowest-longitude sightlines at $\ell = 30^\circ$, we find a very high number of extremely reddened giants in addition to an unreddened population of foreground dwarfs. In contrast to the sightline at $\ell = 45^\circ$, there is no clear group of giant stars visible in the colour-magnitude diagram of Fig. 17, although the red clump stars are manifest as a track of slight over-density sitting roughly 0.4 mag redder than the A0V reddening track. At $(l, b) = (45^\circ, +2^\circ)$ the giant stars observed exhibit a relatively narrow range of extinctions as they lie beyond most of the Galactic dust column. At $(l, b) = (30^\circ, 0^\circ)$ this is not the case: even at the substantial distances at which we can observe reddened giant stars, extinction is continuing to rise within the Galactic mid-plane. It is also apparent that the $(r - i)$ width of both the M dwarfs and early A dwarfs is greater than that in Fig. 16. This is indicative of a steeper rise in reddening, both within several hundred parsecs (M dwarfs) and within a few kpc (early A dwarfs).

These are just descriptive vignettes of the information obtainable from IPHAS colour-colour and colour-magnitude plots. A more rigorous quantitative analysis of the IPHAS catalogue can be undertaken to estimate both the stellar density distribution in the Milky Way (Sale et al. 2010) and to create detailed three-dimensional maps of the extinction across several kpc (Sale et al. 2009; Sale 2012). A 3-D extinction map based on the DR2 catalogue is being released in a separate paper (Sale et al. 2014).

7.2 Identifying H α emission-line objects

An aim of IPHAS is to enable the discovery of new fainter emission-line objects across the Galactic Plane. The survey-wide identification and analysis of emission-line objects is beyond the scope of the present work and will be the focus of a forthcoming paper (Barentsen et al, in preparation). In this section we merely aim to demonstrate a use of the catalogue for this purpose.

An initial list of candidate H α -emitters based on the first IPHAS data release was previously presented by Witham et al. (2008). Because no global calibration was available at the time, Witham et al. employed a sigma-clipping technique to select objects with large, outlying $(r - \text{H}\alpha)$ colours. In contrast, the new catalogue allows objects to be picked out from the $(r - \text{H}\alpha, r - i)$ colour-colour diagram using model-based colour criteria rather than an adaptive statistical procedure. In what follows we demonstrate this new capability by selecting candidate emission-line objects towards a small region in the sky.

The target of our demonstration is Sh 2-82: a 5 arcmin-wide HII region located near $(l, b) = (53.55^\circ, 0.00^\circ)$ in the constellation of Sagitta. Nicknamed by amateur astronomers as the ‘Little Cocoon Nebula’, Sh 2-82 is ionised by the ~ 10 th magnitude star HD 231616 with spectral type

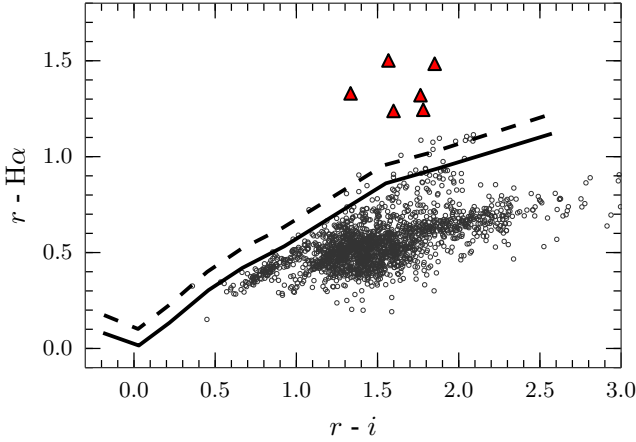


Figure 20. ($r - H\alpha$, $r - i$) diagram for the rectangular region of 20-by-15 arcmin centred on the HII region Sh 2-82, which is the area shown in Fig. 18. The diagram shows all objects in the catalogue which have been flagged as $a10$ and are brighter than $r < 20$ (grey circles). The unreddened main sequence is indicated by a solid line, while the main sequence for stars with an $H\alpha$ emission line strength of -10 \AA EW is indicated by a dashed line (both based on the colour simulations by Barentsen et al. 2011). Red triangles indicate objects which have been identified as likely $H\alpha$ -emitters.

B0V/III (Georgelin et al. 1973; Mayer & Macák 1973; Hunter & Massey 1990). This ionising star has been placed at a likely distance of 1.5–1.7 kpc based on its photometric parallax (Mayer & Macák 1973; Lahulla 1985; Hunter & Massey 1990).

Fig. 18 shows a 20-by-15 arcmin colour mosaic centred on Sh 2-82, composed of our $H\alpha$ (red channel), r (green channel), and i (blue channel) images. The ionising star can be seen as the bright object in the centre of the HII region, which is surrounded by a faint reflection nebula and several dark cloud filaments. For comparison, Fig. 19 shows a mosaic of the same region as seen in the mid-infrared by the Spitzer Space Telescope (Benjamin et al. 2003; Churchwell et al. 2009). The infrared image reveals an enclosing fuzzy bubble (appearing green in Fig. 19) which is thought to originate from the mid-infrared emission of Polycyclic Aromatic Hydrocarbons (PAHs) – i.e. warm dust – which is frequently observed at the interface between neutral regions of interstellar material and the ionising radiation from early-type stars (Churchwell et al. 2006). Yu & Wang (2012) recently noted that the warm dust surrounding Sh 2-82 appears to contain infrared-bright Young Stellar Objects (YSOs). Many of these young objects appear as red- and pink-coloured stars in Fig. 19, located predominantly in the top-left part of the bubble.

Fig. 20 presents the IPHAS colour-colour diagram for the 20-by-15 arcmin region shown in the mosaics. Grey circles show all objects which are brighter than $r < 20$ and have been flagged as $a10$ in IPHAS DR2. The diagram also shows the unreddened main sequence (solid line) and the expected position of unreddened main-sequence stars with $H\alpha$ in emission at a strength of $EW = -10 \text{ \AA}$ (dashed line). Six stars are found to lie above the dashed line at the level of 3σ , i.e. the distance between the objects and the dashed line

Table 9. Candidate $H\alpha$ -emitters towards Sh 2-82.

| # | Name [IPHAS2 ...] | r | i | $H\alpha$ |
|---|---------------------|------------------|------------------|------------------|
| 1 | J192954.40+181026.1 | 17.69 ± 0.01 | 16.12 ± 0.01 | 16.19 ± 0.01 |
| 2 | J193011.01+182051.2 | 18.55 ± 0.02 | 16.95 ± 0.02 | 17.31 ± 0.02 |
| 3 | J193021.52+181954.5 | 19.72 ± 0.05 | 17.94 ± 0.03 | 18.47 ± 0.04 |
| 4 | J193024.45+181938.3 | 19.31 ± 0.04 | 17.55 ± 0.02 | 17.99 ± 0.03 |
| 5 | J193033.00+181609.3 | 18.25 ± 0.01 | 16.91 ± 0.01 | 16.92 ± 0.01 |
| 6 | J193042.48+182317.4 | 19.96 ± 0.03 | 18.11 ± 0.03 | 18.48 ± 0.03 |

is larger than three times the uncertainty in their ($r - H\alpha$) colour. These candidate $H\alpha$ -emitters are marked by red triangles in the colour-colour diagram, and by yellow triangles in the image mosaic (Fig. 18). Their details are listed in Table 9.

In previous work, we have shown that the majority of $H\alpha$ -emitters seen by IPHAS towards an HII region are likely to be Classical T Tauri Stars (Barentsen et al. 2011). These are young objects which are thought to show $H\alpha$ in emission due to the presence of hot, infalling gas which is accreting onto the star from a circumstellar disk. This is likely to be the case for the candidate $H\alpha$ -emitters we discovered towards Sh 2-82 as well. Two of our candidates, #1 and #4 in Table 9, have previously been identified as candidate YSOs by Robitaille et al. (2008) and Yu & Wang (2012), respectively. In these studies, the authors used Spitzer data to find intrinsically red objects, with SEDs consistent with the presence of a circumstellar disk. Although the other four candidate emitters in our sample have not previously appeared in the literature, we note that all four are detected in the Spitzer 8.0 μm image at $S/N > 5$. They are likely to be YSOs exhibiting a mild infrared excess. The recovery of $H\alpha$ -emitters in Spitzer data illustrates how IPHAS can complement infrared surveys.

7.3 IPHAS as a complement to infrared data

Towards Sh2-82, the IPHAS and Spitzer/GLIMPSE catalogues have 4798 entries in common, out of 10 739 and 11 321 entries in total, respectively. 1356 objects of these objects were detected in all four GLIMPSE bands. Fig. 21 presents their colour-colour diagram, in which we have indicated the 845 objects (62 per cent) that have a counterpart in IPHAS (grey circles), and the 511 objects that do not (red crosses).

We find that objects located in the upper half of the Spitzer diagram are less likely to have an IPHAS counterpart, which is where highly-reddened objects are expected to sit. This is not surprising, because Sh2-82 is located towards a high-extinction sightline near the inner plane, where an optical survey will naturally be extinction-limited. Nevertheless, the extinction map due to Sale et al. (2014) has demonstrated that IPHAS can probe stars as far away as 4–5 kpc towards this region. The situation will be even more favourable in the outer-plane, where dust optical depths are low.

We note that Sh 2-82 is one of a large population of poorly-studied star-forming regions located at low Galactic latitudes, which have only recently started to become revealed by efforts to catalogue the wealth of ‘bubbles’ detected at mid-infrared

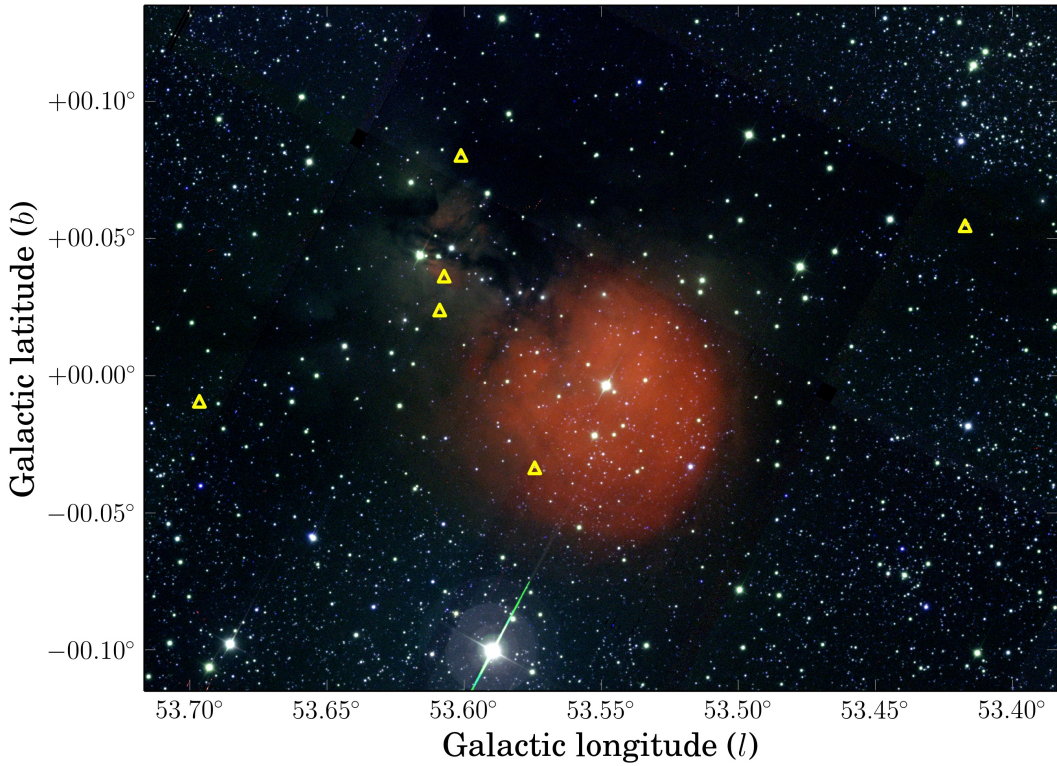


Figure 18. IPHAS image mosaic of HII region Sh 2-82, composed of H α (red channel), r (green channel) and i (blue channel). Yellow triangles show the position of candidate H α -emitters which have been selected from the colour-colour diagram in Fig. 20.

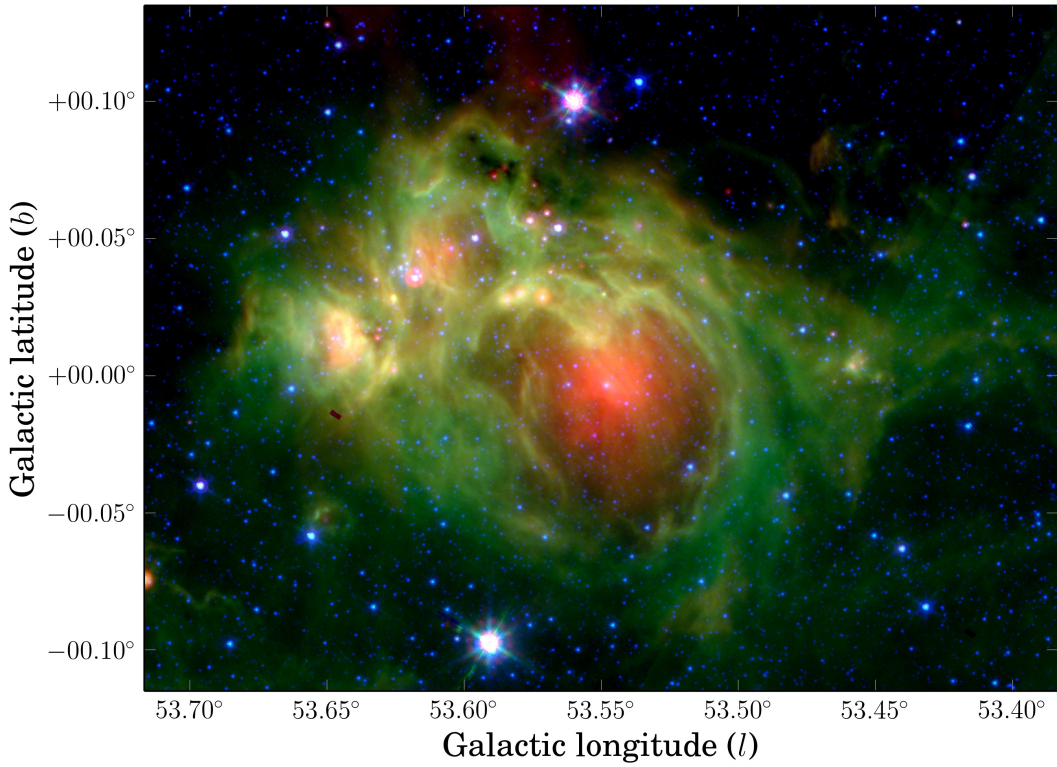


Figure 19. Star-forming region Sh 2-82 as seen in the mid-infrared by the Spitzer Space Telescope. The mosaic is composed of the 24 μm (red), 8.0 μm (green) and 4.5 μm (blue) bands. The image reveals a bubble-shaped structure which surrounds the HII region that is seen in the IPHAS mosaic which spans the same region (Fig. 18). This structure has previously been labelled as N115 in the catalogue of Churchwell et al. (2006), and could be a possible site of triggered star formation (Thompson et al. 2012; Kendrew et al. 2012).

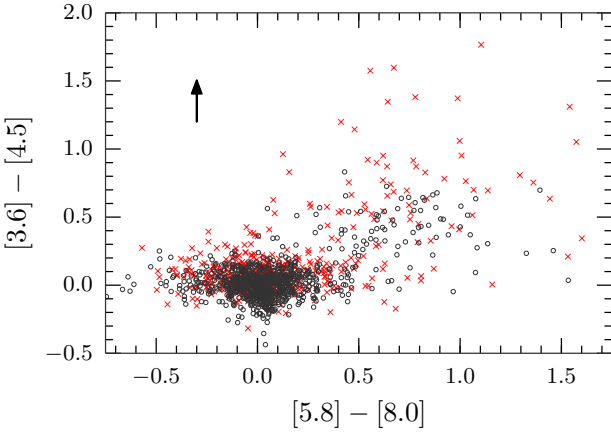


Figure 21. Spitzer/GLIMPSE colour-colour diagram towards Sh 2-82, showing the objects for which a counterpart exists in IPHAS (845 objects, grey circles) and those for which no counterpart was identified (511 objects, red crosses). A cross-matching radius of 1 arcsec was used to identify counterparts. The arrow illustrates the reddening vector corresponding to $A_{Ks} = 3$ following the reddening law due to Flaherty et al. (2007). It is apparent that the most heavily reddened objects tend to have no counterpart. Three heavily-reddened objects without counterpart are located above the diagram but are not shown for clarity.

wavelengths (Churchwell et al. 2006; Simpson et al. 2012), and by efforts to catalogue previously unknown clusters seen in the near-infrared (e.g. Bica et al. 2003). IPHAS data can offer a handle on the extinction, distance and stellar contents of many of such unexplored regions.

7.4 $r - H\alpha$ excess as a quantitative measure of $H\alpha$ emission

As well as discover emission line stars, IPHAS data can provide a first estimate of the equivalent width of line emission. How this is done has been discussed in previous works – most notably by Drew et al. (2005) and more recently by Barentsen et al. (2011). Given that the narrowband filter used has a FWHM of 95 Å, it is to be expected that the appearance in a spectrum of line emission corresponding to an equivalent width (EW) of 95 Å would increase $r - H\alpha$ by 0.75 magnitudes (i.e. the flux captured within the narrow band doubles). Similarly, 10 Å of line emission should increase $r - H\alpha$ by 0.11 mag.

This simple reasoning breaks down when the $H\alpha$ emission becomes so bright that it also dominates the flux captured across the entire r broadband. It was noted by Drew et al. (2005) that the very bright line limiting value of $r - H\alpha$ is ~ 3.1 in the Vega system. This fact, on its own, implies that any apparent detection of an $H\alpha$ emission line star without a corresponding r detection is only real if the $H\alpha$ magnitude is not brighter by more than 3.1 mag relative to the r detection limit (i.e. typically, credible $H\alpha$ -only sources must be fainter than ~ 18 th mag).

In order to infer the emission EW from the DR2 $r - H\alpha$ colour it is necessary to know the value this

colour would have in the case of no excess line emission. In the *general* case this is not possible without some prior knowledge of the star’s reddening and spectral type (i.e. the inferences drawn for an unreddened M dwarf or a reddened F star would not be the same – the absolute value of the equivalent width in the latter case would be greater because the reddened F star *without* emission would lie at lower $r - H\alpha$). This is the situation faced in the study of IC 1396 by Barentsen et al. (2011) in which $H\alpha$ EWs were inferred relative to a reddened sequence of K-M stars appropriate to this star-forming region. A different choice of reddening would have resulted in different EW estimates.

However it was found by Drew et al. (2005) that for earlier type stars in which the spectrum is not heavily modulated by line features or molecular bands the estimation of net emission EW is more straightforward and unambiguous. It was demonstrated, for spectral slopes ranging from the Rayleigh-Jeans limit to that appropriate to an early G star and for a range of reddenings, that it is possible to draw a unique set of constant equivalent-width lines in the $(r - H\alpha, r - i)$ diagram that can be compared directly with the positions of candidate emission line stars, thereby predicting emission EW (see fig. 6, Drew et al. 2005). The EW in this case should be understood to be the measure of the emission observed above the interpolated continuum (i.e. no correction is present for any assumed infilled photospheric line absorption).

In Fig. 22 we show how well this works in reality: the predicted lines of constant emission EW in the $(r - H\alpha, r - i)$ plane are compared with the positions of a sample of over 200 classical Be stars in Perseus (from Raddi et al. 2014). Stars of this type come with the advantage that secular variation, whilst it certainly occurs, is not as common as in T Tau stars. The objects plotted are a bright selection ($r \lesssim 16.5$) for which there are spectroscopic determinations of $H\alpha$ emission equivalent width. A colour scale has been applied to the data points that darkens as EW increases. The gradation apparent in the shading of the datapoints follows the trend set by the constant EW lines quite well. The experience has been that the EW deduced from IPHAS photometry for individual objects is commonly within 10 Å of subsequent spectroscopic measurement (see also fig. 5 of Barentsen et al. 2011). Evidently, the photometry is well-suited to statistical measurement across large samples, while for individual objects a useful approximation is delivered.

8 CATALOGUE AND IMAGE ACCESS

The catalogue will be made available through the Vizier service (<http://vizier.u-strasbg.fr>), where it can be queried using a web interface and using Virtual Observatory (VO) protocols. In addition, the catalogue can be downloaded in its entirety from our website as a collection of binary FITS

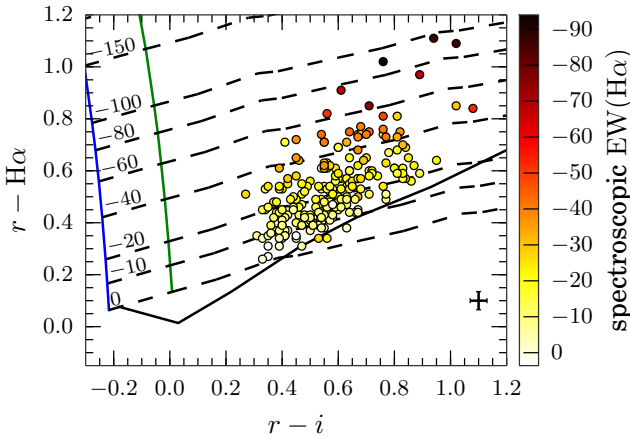


Figure 22. Photometric predictions of $\text{H}\alpha$ equivalent width (EW) compared with spectroscopic measurements of a sample of classical Be stars (from Raddi et al 2014, submitted). The broken lines are predicted lines of constant net emission EW, while the analogous spectroscopic EW is represented by the colouring of the data points. The unreddened main sequence, which normally serves as the upper bound to the main stellar locus, is drawn as a solid black line. Strongly reddened stars with not-so-strong line emission will fall below it and be hard to pick out without additional information. The two vertical lines drawn are ‘curves of growth’ showing how $r - \text{H}\alpha$ increases – and $r - i$ drops a little – as more and more line emission is added, raising the flux in $\text{H}\alpha$ narrowband and to a lesser proportion the flux in the r band. The blue line represents the trend for an unreddened Rayleigh-Jeans continuum (with superposed $\text{H}\alpha$ emission), while the green line is the trend for the case of an unreddened A0 continuum.

tables, each covering a $5^\circ \times 5^\circ$ tile of the footprint and comprising 50 gigabyte in total (see www.iphas.org/dr2).

We do not recommend using the catalogue to study extended objects which are larger than the aperture diameters specified in this work. To enable the analysis of diffuse sources, our website provides access to the entire set of pipeline-processed imaging data and associated meta data (see www.iphas.org/images). The image headers have been updated to include a new keyword, called PHOTZP, which contains the re-calibrated zeropoint. This keyword can be used to convert the number counts DN , i.e. the pixel values in the images, into Vega-based magnitudes m using:

$$m = \text{PHOTZP} - 2.5 \log_{10}(DN). \quad (11)$$

The PHOTZP value has been computed such that it absorbs the required corrections for atmospheric extinction, gain variations, exposure time, and the re-calibration shift. As these images still include moonlight and other sources of non-astronomical background, they can only support flux measurements that include a suitably-chosen local background subtraction.

To estimate absolute narrow-band $\text{H}\alpha$ fluxes from the image data, we note that the integrated in-band energy flux for Vega in the IPHAS $\text{H}\alpha$ filter is 1.52×10^{-7} erg cm $^{-2}$ s $^{-1}$ at the top of the Earth’s atmosphere, which is the flux obtained by folding the CALSPEC SED with the filter transmission curve only (the correction for atmosphere and detector quantum efficiency, otherwise scales down the nar-

rowband flux by 0.707). This implies that the in-band flux corresponding to zero magnitude is 1.56×10^{-7} erg cm $^{-2}$ s $^{-1}$, when the $\text{H}\alpha$ magnitude for Vega is set by convention to 0.03 (Fukugita et al. 1996). These flux estimates are consistent with the most recent version of Vega’s SED presented by Bohlin (2014).

We warn that the image repository on our website includes data that did not pass quality control and has not been globally re-calibrated. Such data are flagged **in the on line meta data table, which is available from our website**, and must be used with great caution.

In the spirit of reproducibility, the source code that was used to generate the catalogue is made available at <https://github.com/barentsen/iphas-dr2>

9 CONCLUDING REMARKS AND FUTURE WORK

A new catalogue has been derived from the INT/WFC Photometric $\text{H}\alpha$ Survey of the Northern Galactic Plane. It is the first to offer comprehensive CCD photometry of point sources across the Northern Galactic Plane at visible wavelengths, taking in the Galactic latitude range $|b| < 5^\circ$ at longitudes $\ell = 30^\circ$ to 215° . The new 99-column catalogue provides single-epoch photometry across 92 per cent of the survey area, and is the first quality-controlled and globally calibrated catalogue to have been constructed from the imaging data. This now means that there is $\text{H}\alpha$ coverage, accessible online, of the entire Galactic Plane – given that the southern Plane is already available thanks to the UK Schmidt $\text{H}\alpha$ Survey (SHS, Parker et al. 2005), the last of the photographic surveys carried out by that telescope.

The observations included in this release achieve a median seeing of 1.1 arcsec and 5σ -depths of $r = 21.2 \pm 0.5$, $i = 20.0 \pm 0.3$, and $\text{H}\alpha = 20.3 \pm 0.3$. The global calibration and photometric repeatability are found to be accurate at the level of 0.03 mag (rms), providing a significant improvement over the previous data release. The source catalogue specifies the best-available single-epoch astrometry and photometry for 219 million unique sources. To support its exploitation, we provide a list of recommended quality criteria that will permit the selection of objects with accurate colours from the catalogue. The closing demonstrations highlight the use of the survey’s unique $(r - \text{H}\alpha, r - i)$ diagram for characterising stellar populations and selecting emission-line objects. More comprehensive applications of IPHAS can be found in the works of Sale et al. (2014), which applies DR2 to the problem of 3D extinction mapping, and of Sabin et al. (2014), where the results of a search of the image database for new planetary nebulae is presented.

The current plan is to work toward one further major IPHAS source catalogue, in which the remaining gaps in sky coverage will have been eliminated – observations aimed at replacing data not meeting the quality requirements are continuing. We will also examine options to further improve the global calibration, perhaps tightening the accuracy to better than 2 per cent. For example, we have in mind investigating the use of the PanSTARRS photometric ladder (Magnier et al. 2013) as a reference set, when it becomes available for the Galactic Plane, and we will explore improving source

recovery in the most dense fields via the implementation of PSF fitting in place of aperture photometry. Finally, the next catalogue will detail all the secondary detections to aid time-domain studies.

The data-taking strategy developed for IPHAS has since been reapplied to carry out a companion INT/WFC Galactic Plane survey called UVEX in U , g , r , He I (Groot et al. 2009), a survey of the Kepler field in U , g , r , i , $\text{H}\alpha$ (Greiss et al. 2012), and a survey of the Southern Galactic Plane and Bulge in u , g , r , i , $\text{H}\alpha$ called VPHAS+ (Drew et al. 2014). The last of these incorporates the digital update of the SHS, offering all the advantages of calibrated photometry across a little over half the SHS footprint. The work presented here stands as a potential template for the catalogues that remain to be generated from these sibling surveys. In prospect from them, whether they are mined separately or together, are the means to ask seamless questions on the contents and structure of the most highly-populated components of the Milky Way.

ACKNOWLEDGMENTS

The INT is operated on the island of La Palma by the Isaac Newton Group (ING) in the Spanish Observatorio del Roque de los Muchachos of the Instituto de Astrofísica de Canarias. We are deeply indebted to Ovidiu Vaduvescu, Javier Méndez and the rest of the ING staff and students for their ongoing support of the telescope. All data were processed by the Cambridge Astronomical Survey Unit at the Institute of Astronomy in Cambridge. The catalogue presented in this work was assembled at the Centre for Astrophysics Research, University of Hertfordshire, supported by a grant from the Science & Technology Facilities Council of the UK (STFC, ref ST/J001335/1).

Preparation of the catalogue was eased greatly by a number of software packages, including the POSTGRESQL database software, the TOPCAT and STILTS packages (Taylor 2005, 2006), and the Python modules ASTROPY (Astropy Collaboration et al. 2013), NUMPY and SCIPY (Oliphant 2007), MATPLOTLIB (Hunter 2007), IPYTHON (Pérez & Granger 2007), and APLPY. We also made use of the MONTAGE software maintained by NASA/IPAC, and the SIMBAD, VIZIER and ALADIN services operated at CDS, Strasbourg, France (Bonnarel et al. 2000).

Our work made extensive use of several complementary photometric surveys. Our global calibration was aided by the AAVSO Photometric All-Sky Survey (APASS), funded by the Robert Martin Ayers Sciences Fund. The calibration was tested against the Sloan Digitized Sky Survey (SDSS), funded by the Alfred P. Sloan Foundation, the Participating Institutions, the National Science Foundation, the U.S. Department of Energy, the National Aeronautics and Space Administration, the Japanese Monbukagakusho, the Max Planck Society, and the Higher Education Funding Council for England. The astrometric pipeline reduction made significant use of the Two Micron All Sky Survey (2MASS), which is a joint project of the University of Massachusetts and the Infrared Processing and Analysis Center/ California Institute of Technology, funded by NASA and the NSF. This work includes observations made with the Spitzer Space Telescope, which is operated by the Jet Propulsion Laboratory,

California Institute of Technology under a contract with NASA.

GB, JED, SES and BTG acknowledge support from the Science & Technology Facilities Council of the United Kingdom (grants: GB and JED ST/J001333/1, SES ST/K00106X/1, BTG ST/I001719/1). HJF and MM-S both acknowledge STFC postgraduate studentships. JED would also like to convey her thanks to the Physics Department of Imperial College London that hosted this project from its inception to 2007 and supported her via a sabbatical year in 2003-4. JF is supported by the Spanish Plan Nacional de I+D+i and FEDER under contract AYA2010-18352. BTG acknowledges funding from the European Research Council under the European Union's Seventh Framework Programme (FP/2007-2013) / ERC Grant Agreement n. 320964 (WDTracer). PRG is supported by a Ramón y Cajal fellowship (RYC-2010-05762), and acknowledges support provided by the Spanish MINECO AYA2012-38700 grant. NJW is in receipt of a Fellowship funded by the Royal Astronomical Society of the United Kingdom.

We are grateful to the anonymous referee for the insightful feedback, which has helped us to improve the presentation of the data products.

REFERENCES

- Ahn C. P. et al., 2012, ApJS, 203, 21
- Astropy Collaboration et al., 2013, A&A, 558, A33
- Aungwojwit A., Gänsicke B. T., Wheatley P. J., Pyrzas S., Staels B., Krajci T., Rodríguez-Gil P., 2012, ApJ, 758, 79
- Barentsen G. et al., 2011, MNRAS, 415, 103
- Barentsen G., Vink J. S., Drew J. E., Sale S. E., 2013, MNRAS, 429, 1981
- Benjamin R. A. et al., 2003, PASP, 115, 953
- Bessell M., Murphy S., 2012, PASP, 124, 140
- Bica E., Dutra C. M., Soares J., Barbuy B., 2003, A&A, 404, 223
- Bohlin R. C., 2014, ArXiv e-prints
- Bok B. J., Bok P., 1941, The Milky way
- Bonnarel F. et al., 2000, A&AS, 143, 33
- Bressan A., Marigo P., Girardi L., Salasnich B., Dal Cero C., Rubel S., Nanni A., 2012, MNRAS, 427, 127
- Calabretta M. R., Greisen E. W., 2002, A&A, 395, 1077
- Churchwell E. et al., 2009, PASP, 121, 213
- Churchwell E. et al., 2006, ApJ, 649, 759
- Corradi R. L. M. et al., 2008, A&A, 480, 409
- Corradi R. L. M., Sabin L., Munari U., Cetrulo G., Englareo A., Angeloni R., Greimel R., Mampaso A., 2011, A&A, 529, A56
- Corradi R. L. M. et al., 2010, A&A, 509, A41
- Cross N. J. G. et al., 2012, A&A, 548, A119
- Drew J. E. et al., 2014, MNRAS, 440, 2036
- Drew J. E. et al., 2005, MNRAS, 362, 753
- Drew J. E., Greimel R., Irwin M. J., Sale S. E., 2008, MNRAS, 386, 1761
- Finkbeiner A., 2010, A Grand and Bold Thing: An Extraordinary New Map of the Universe Ushering. Free Press
- Flaherty K. M., Pipher J. L., Megeath S. T., Winston E. M., Gutermuth R. A., Muzerolle J., Allen L. E., Fazio G. G., 2007, ApJ, 663, 1069
- Fukugita M., Ichikawa T., Gunn J. E., Doi M., Shimasaku K., Schneider D. P., 1996, AJ, 111, 1748
- Georgelin Y. M., Georgelin Y. P., Roux S., 1973, A&A, 25, 337
- Giammanco C. et al., 2011, A&A, 525, A58
- Glazebrook K., Peacock J. A., Collins C. A., Miller L., 1994, MNRAS, 266

- González-Solares E. A. et al., 2011, MNRAS, 416, 927
 González-Solares E. A. et al., 2008, MNRAS, 388, 89
 Greiss S. et al., 2012, AJ, 144, 24
 Groot P. J. et al., 2009, MNRAS, 399, 323
 Hambly N. C. et al., 2008, MNRAS, 384, 637
 Henden A. A., Levine S. E., Terrell D., Smith T. C., Welch D., 2012, Journal of the American Association of Variable Star Observers (JAAVSO), 40, 430
 Hunter D. A., Massey P., 1990, AJ, 99, 846
 Hunter J. D., 2007, Computing In Science & Engineering, 9, 90
 Irwin M., Lewis J., 2001, New Astronomy Reviews, 45, 105
 Irwin M., McMahon R., Walton N., González-Solares E., Hodgkin S., Irwin J., Lewis J., 2005, The Newsletter of the Isaac Newton Group of Telescopes, 9, 8
 Irwin M. J., 1985, MNRAS, 214, 575
 Irwin M. J., 1997, Detectors and data analysis techniques for wide field optical imaging., Rodríguez Espinosa J. M., Herrero A., Sánchez F., eds., pp. 35–74
 Ivezić Ž. et al., 2007, AJ, 134, 973
 Kendrew S. et al., 2012, ApJ, 755, 71
 Kohoutek L., Wehmeyer R., 1999, A&AS, 134, 255
 Lahulla J. F., 1985, A&AS, 61, 537
 Landolt A. U., 1992, AJ, 104, 340
 Lawrence A. et al., 2007, MNRAS, 379, 1599
 Lucas P. W. et al., 2008, MNRAS, 391, 136
 Magnier E. A. et al., 2013, ApJS, 205, 20
 Mampaso A. et al., 2006, A&A, 458, 203
 Manfroid J., 1995, A&AS, 113, 587
 Mayer P., Macák P., 1973, Bulletin of the Astronomical Institutes of Czechoslovakia, 24, 50
 McMahon R. G., Walton N. A., Irwin M. J., Lewis J. R., Bunclark P. S., Jones D. H., 2001, New Astronomy Reviews, 45, 97
 Minniti D. et al., 2010, New A, 15, 433
 Nikolaev S., Weinberg M. D., Skrutskie M. F., Cutri R. M., Wheelock S. L., Gizis J. E., Howard E. M., 2000, AJ, 120, 3340
 Oliphant T. E., 2007, Computing in Science & Engineering, 9, 10
 Padmanabhan N. et al., 2008, AJ, 674, 1217
 Parker Q. A. et al., 2005, MNRAS, 362, 689
 Pérez F., Granger B. E., 2007, Computing in Science and Engineering, 9, 21
 Pickles A. J., 1998, PASP, 110, 863
 Raddi R. et al., 2013, MNRAS, 430, 2169
 Robitaille T. P. et al., 2008, AJ, 136, 2413
 Rodríguez-Flores E. R., Corradi R. L. M., Mampaso A., García-Alvarez D., Munari U., Greimel R., Rubio-Díez M. M., Santander-García M., 2014, A&A, 567, A49
 Sabin L. et al., 2013, MNRAS, 431, 279
 Sabin L. et al., 2014, ArXiv e-prints
 Sabin L., Zijlstra A. A., Wareing C., Corradi R. L. M., Mampaso A., Viironen K., Wright N. J., Parker Q. A., 2010, PASA, 27, 166
 Sale S. E., 2012, MNRAS, 427, 2119
 Sale S. E. et al., 2014, ArXiv e-prints
 Sale S. E. et al., 2010, MNRAS, 402, 713
 Sale S. E. et al., 2009, MNRAS, 392, 497
 Schlafly E. F., Finkbeiner D. P., 2011, ApJ, 737, 103
 Schlafly E. F. et al., 2012, ApJ, 756, 158
 Schlegel D. J., Finkbeiner D. P., Davis M., 1998, ApJ, 500, 525
 Simpson R. J. et al., 2012, MNRAS, 424, 2442
 Skrutskie M. F. et al., 2006, AJ, 131, 1163
 Taylor M. B., 2005, in Astronomical Society of the Pacific Conference Series, Vol. 347, Astronomical Data Analysis Software and Systems XIV, Shopbell P., Britton M., Ebert R., eds., p. 29
 Taylor M. B., 2006, in Astronomical Society of the Pacific Conference Series, Vol. 351, Astronomical Data Analysis Software and Systems XV, Gabriel C., Arviset C., Ponz D., Enrique S., eds., p. 666
 Thompson M. A., Urquhart J. S., Moore T. J. T., Morgan L. K., 2012, MNRAS, 421, 408
 Viironen K. et al., 2009a, A&A, 504, 291
 Viironen K. et al., 2011, A&A, 530, A107
 Viironen K. et al., 2009b, A&A, 502, 113
 Vink J. S., Drew J. E., Steeghs D., Wright N. J., Martin E. L., Gänsicke B. T., Greimel R., Drake J., 2008, MNRAS, 387, 308
 Wesson R. et al., 2008, ApJ, 688, L21
 Witham A. R. et al., 2007, MNRAS, 382, 1158
 Witham A. R., Knigge C., Drew J. E., Greimel R., Steeghs D., Gänsicke B. T., Groot P. J., Mampaso A., 2008, MNRAS, 384, 1277
 Wright N. J., Drake J. J., Drew J. E., Guarcello M. G., Gutermuth R. A., Hora J. L., Kraemer K. E., 2012, ApJ, 746, L21
 Wright N. J. et al., 2008, MNRAS, 390, 929
 Yanny B. et al., 2009, AJ, 137, 4377
 Yu N.-P., Wang J.-J., 2012, Research in Astronomy and Astrophysics, 12, 651
 Zacharias N. et al., 2010, AJ, 139, 2184
 Zacharias N., Finch C. T., Girard T. M., Henden A., Bartlett J. L., Monet D. G., Zacharias M. I., 2013, AJ, 145, 44

APPENDIX A: CATALOGUE FORMAT

Table A1: Definition of columns in the IPHAS DR2 source catalogue.

| # | Column | Type | Unit | Description |
|----|-----------------|---------|---------|--|
| 1 | name | string | | Position-based source name in the sexagesimal form: "JHH-MMSS.ss+DDMMSS.s". You need to add the prefix "IPHAS2" followed by a whitespace to obtain the official name "IPHAS2 JHHMMSS.ss+DDMMSS.s" (where "J" indicates that the position is J2000 equatorial and "IPHAS2" indicates DR2). |
| 2 | ra | double | degrees | J2000 Right Ascension with respect to the 2MASS PSC reference frame, which is consistent with ICRS to within 0.1 arcsec. The coordinate given is obtained from the astrometric measurement in the r-band exposure. If the source is undetected in r, then the i or H α -band coordinate is given. |
| 3 | dec | double | degrees | J2000 Declination. See comments above. |
| 4 | sourceID | string | | Unique identification number of the detection. Identical to rDetectionID if the source was detected in the r-band. Identical to iDetectionID or haDetectionID otherwise. |
| 5 | posErr | float | arcsec | Astrometric root mean square (RMS) residual measured against 2MASS across the CCD in which the source is detected. Be aware that the astrometric error for a source near the corner of a CCD may be significantly larger than the RMS statistic. |
| 6 | l | double | degrees | Galactic longitude ℓ converted from ra/dec (IAU 1958 system). |
| 7 | b | double | degrees | Galactic latitude b converted from ra/dec (IAU 1958 system). |
| 8 | mergedClass | short | | Image classification flag based on all bands: 1=galaxy, 0=noise, -1=star, -2=probableStar, -3=probableGalaxy, -9=saturated. Computed using the UKIDSS scheme. |
| 9 | mergedClassStat | float | | Merged N(0,1) stellarness-of-profile statistic. Computed using the UKIDSS scheme. |
| 10 | pStar | float | | Probability that the source is a point source (value between 0 and 1). |
| 11 | pGalaxy | float | | Probability that the source is an extended object, such as a galaxy, or a close blend of two point sources (value between 0 and 1). |
| 12 | pNoise | float | | Probability that the source is noise, e.g. a cosmic ray (value between 0 and 1). |
| 13 | rmi | float | mag | (r - i) colour, formed by subtracting columns r and i. To obtain the uncertainty, take the root of the sum of the squares of columns rErr and iErr. |
| 14 | rmha | float | mag | (r - H α) colour, formed by subtracting columns r and ha. See comments above. |
| 15 | r | float | mag | Default r-band magnitude using the 2.3 arcsec diameter aperture. Calibrated in the Vega system. |
| 16 | rErr | float | mag | Uncertainty for r. Does not include systematic errors. |
| 17 | rPeakMag | float | mag | Alternative r-band magnitude derived from the peak pixel height (i.e. a 0.3x0.3 arcsec square aperture). Calibrated in the Vega system. |
| 18 | rPeakMagErr | float | mag | Uncertainty in rPeakMag. Does not include systematics. |
| 19 | rAperMag1 | float | mag | Alternative r-band magnitude using the 1.2 arcsec diameter aperture. Calibrated in the Vega system. |
| 20 | rAperMag1err | float | mag | Uncertainty in rAperMag1. Does not include systematics. |
| 21 | rAperMag3 | float | mag | Alternative r-band magnitude using the 3.3 arcsec diameter aperture. Calibrated in the Vega system. |
| 22 | rAperMag3err | float | mag | Uncertainty in rAperMag3. Does not include systematics. |
| 23 | rGauSig | float | pixels | RMS of axes of ellipse fit in r. |
| 24 | rEll | float | | Ellipticity in the r-band. |
| 25 | rPA | float | | Position angle in the r-band. |
| 26 | rClass | short | | Discrete image classification flag: 1=galaxy, 0=noise, -1=star, -2=probableStar, -3=probableGalaxy, -9=saturated. |
| 27 | rClassStat | float | | N(0,1) stellarness-of-profile statistic. |
| 28 | rDeblend | boolean | | True if the source is blended with a nearby neighbour in the r-band. Although a deblending procedure is applied when measuring the photometry, the result may be unreliable (colours should not be trusted in particular). |
| 29 | rSaturated | boolean | | True if the source is too bright to make an accurate measurement in the r-band (e.g. peak pixel > 55000 counts). The photometry is likely affected by systematic errors. |
| 30 | rMJD | double | days | Modified Julian Date at the start of the r-band exposure. |
| 31 | rSeeing | float | arcsec | Average Full Width at Half Maximum (FWHM) of stars in the same CCD frame. |
| 32 | rDetectionID | string | | Unique identifier of the r-band detection in the format "#run-#ccd-number", i.e. composed of the INT telescope run number, the CCD number and a sequential source detection number. |

Table A1 – continued

| # | Column | Type | Unit | Description |
|----|---------------|---------|---------|---|
| 33 | rX | float | pixels | Pixel coordinate of the source in the r-band exposure, in the coordinate system of the CCD. |
| 34 | rY | float | pixels | Pixel coordinate of the source in the r-band exposure, in the coordinate system of the CCD. |
| 35 | i | float | mag | Default i-band magnitude using the 2.3 arcsec diameter aperture. Calibrated in the Vega system. |
| 36 | iErr | float | mag | Uncertainty for i. Does not include systematic errors. |
| 37 | iPeakMag | float | mag | Alternative i-band magnitude derived from the peak pixel height (i.e. a 0.3x0.3 arcsec square aperture). Calibrated in the Vega system. |
| 38 | iPeakMagErr | float | mag | Uncertainty in iPeakMag. Does not include systematics. |
| 39 | iAperMag1 | float | mag | Alternative i-band magnitude using the 1.2 arcsec diameter aperture. Calibrated in the Vega system. |
| 40 | iAperMag1err | float | mag | Uncertainty in iAperMag1. Does not include systematics. |
| 41 | iAperMag3 | float | mag | Alternative i-band magnitude using the 3.3 arcsec diameter aperture. Calibrated in the Vega system. |
| 42 | iAperMag3err | float | mag | Uncertainty in iAperMag3. Does not include systematics. |
| 43 | iGauSig | float | pixels | RMS of axes of ellipse fit. |
| 44 | iEll | float | | Ellipticity. |
| 45 | iPA | float | degrees | Position angle. |
| 46 | iClass | short | | Discrete image classification flag: 1=galaxy, 0=noise, -1=star, -2=probableStar, -3=probableGalaxy, -9=saturated. |
| 47 | iClassStat | float | | N(0,1) stellarness-of-profile statistic. |
| 48 | iDeblend | boolean | | True if the source is blended with a nearby neighbour in the i-band. See comments for rDeblend above. |
| 49 | iSaturated | boolean | | True if the source is too bright to make an accurate measurement in the i-band. See comments for rSaturated above. |
| 50 | iMJD | double | days | Modified Julian Date at the start of the single-band exposure. |
| 51 | iSeeing | float | arcsec | Average Full Width at Half Maximum (FWHM) of stars in the same CCD frame. |
| 52 | iDetectionID | string | | Unique identifier of the i-band detection in the format "#run-#ccd-number", i.e. composed of the INT telescope run number, the CCD number and a sequential source detection number. |
| 53 | iX | float | pixels | Pixel coordinate of the source, in the coordinate system of the CCD. |
| 54 | iY | float | pixels | Pixel coordinate of the source, in the coordinate system of the CCD. |
| 55 | iXi | float | arcsec | Position offset of the i-band detection relative to the ra column. The original i-band coordinates can be obtained by computing (ra+iXi/3600, dec+iEta/3600). |
| 56 | iEta | float | arcsec | Position offset of the i-band detection relative to the dec column. See comments above. |
| 57 | ha | float | mag | Default H-alpha magnitude using the 2.3 arcsec aperture. Calibrated in the Vega system. |
| 58 | haErr | float | mag | Uncertainty for ha. Does not include systematic errors. |
| 59 | haPeakMag | float | mag | Alternative H-alpha magnitude derived from the peak pixel height (i.e. a 0.3x0.3 arcsec square aperture). Calibrated in the Vega system. |
| 60 | haPeakMagErr | float | mag | Uncertainty in haPeakMag. Does not include systematics. |
| 61 | haAperMag1 | float | mag | Alternative H-alpha magnitude using the 1.2 arcsec diameter aperture. Calibrated in the Vega system. |
| 62 | haAperMag1err | float | mag | Uncertainty in haAperMag1. Does not include systematics. |
| 63 | haAperMag3 | float | mag | Alternative H-alpha magnitude using the 3.3 arcsec diameter aperture. Calibrated in the Vega system. |
| 64 | haAperMag3err | float | mag | Uncertainty in haAperMag3. Does not include systematics. |
| 65 | haGauSig | float | pixels | RMS of axes of ellipse fit. |
| 66 | haEll | float | | Ellipticity. |
| 67 | haPA | float | degrees | Position angle. |
| 68 | haClass | short | | Discrete image classification flag: 1=galaxy, 0=noise, -1=star, -2=probableStar, -3=probableGalaxy, -9=saturated. |
| 69 | haClassStat | float | | N(0,1) stellarness-of-profile statistic. |
| 70 | haDeblend | boolean | | True if the source is blended with a nearby neighbour in H-alpha. See comments for rDeblend above. |
| 71 | haSaturated | boolean | | True if the source is too bright to make an accurate measurement in H-alpha. See comments for rSaturated above. |
| 72 | haMJD | double | days | Modified Julian Date at the start of the single-band exposure. |
| 73 | haSeeing | float | arcsec | Average Full Width at Half Maximum (FWHM) of stars in the same CCD frame. |

Table A1 – continued

| # | Column | Type | Unit | Description |
|----|---------------|---------|--------|--|
| 74 | haDetectionID | string | | Unique identifier of the H-alpha detection in the format "#run#ccd-number", i.e. composed of the INT telescope run number, the CCD number and a sequential source detection number. |
| 75 | haX | float | pixels | Pixel coordinate of the source, in the coordinate system of the CCD. |
| 76 | haY | float | pixels | Pixel coordinate of the source, in the coordinate system of the CCD. |
| 77 | haXi | float | arcsec | Position offset of the H-alpha detection relative to the ra column. The original Ha-band coordinates can be obtained by computing (ra+haXi/3600, dec+haEta/3600). |
| 78 | haEta | float | arcsec | Position offset of the H-alpha relative to the ra column. See comments above. |
| 79 | brightNeighb | boolean | | True if a very bright star is nearby (defined as brighter than V<4 within 10 arcmin, or brighter than V<7 within 5 arcmin). Such very bright stars cause scattered light and diffraction spikes, which may add systematic errors to the photometry or even trigger spurious detections. |
| 80 | deblend | boolean | | True if the source is blended with a nearby neighbour in one or more bands. Although a deblending procedure is applied when measuring the photometry, the result may be inaccurate and the colours should not be trusted. |
| 81 | saturated | boolean | | True if the source is saturated in one or more bands. The photometry of saturated stars is affected by systematic errors. |
| 82 | nBands | short | | Number of bands in which the source is detected (equals 1, 2 or 3). |
| 83 | a10 | boolean | | True if the source is detected at S/N > 10 in all bands without being saturated, and if the photometric measurements are consistent across different aperture diameters. Algebraic condition: (rErr < 0.1 & iErr < 0.1 & haErr < 0.1 & NOT saturated & (abs(r-rAperMag1) < 3*hypot(rErr,rAperMag1Err)+0.03) & (abs(i-iAperMag1) < 3*hypot(iErr,iAperMag1Err)+0.03) & (abs(ha-haAperMag1) < 3*hypot(haErr,haAperMag1Err)+0.03). |
| 84 | a10point | boolean | | True if both the a10 quality criteria above are satisfied, and if the object looks like a single, unconfused point source. Algebraic condition: a10 & pStar > 0.9 & NOT deblend & NOT brightNeighb. |
| 85 | fieldID | string | | Survey field identifier (e.g. 0001_aug2003). |
| 86 | fieldGrade | string | | Internal quality control score of the field. One of A, B, C or D. |
| 87 | night | integer | | Night of the observation (YYYYMMDD). Refers to the UT date at the start of the night. |
| 88 | seeing | float | arcsec | Maximum value of rSeeing, iSeeing, or haSeeing. |
| 89 | ccd | short | | CCD-chip number on the Wide Field Camera (WFC) of the Isaac Newton Telescope (INT). 1, 2, 3 or 4. |
| 90 | nObs | short | | Number of repeat observations of this source in the survey. A value larger than 1 indicates that the source is unlikely to be spurious. |
| 91 | sourceID2 | string | | SourceID of the alternative detection of the object in the partner exposure. |
| 92 | fieldID2 | string | | FieldID of the partner detection (e.g. 0001o_aug2003). |
| 93 | r2 | float | mag | r-band magnitude in the dithered partner field, i.e. the dithered repeat measurement obtained within 10 minutes (if available). |
| 94 | rErr2 | float | mag | Uncertainty for r2. |
| 95 | i2 | float | mag | i-band magnitude in the dithered partner field, i.e. the dithered repeat measurement obtained within 10 minutes (if available). |
| 96 | iErr2 | float | mag | Uncertainty for i2. |
| 97 | ha2 | float | mag | H-alpha magnitude in the dithered partner field, i.e. the dithered repeat measurement obtained within 10 minutes (if available). |
| 98 | haErr2 | float | mag | Uncertainty for ha2. |
| 99 | errBits2 | integer | | Error bitmask for the partner detection. Used to flag a bright neighbour (1), source blending (2), saturation (8), vignetting (64), truncation (128) and bad pixels (32768). Be careful if errBits2 > 0. |